Monthly Notices
of the
ROYAL ASTRONOMICAL SOCIETY

MNRAS **475,** 2768–2786 (2018)
Advance Access publication 2018 January 4

doi:10.1093/mnras/stx3358

A simulation-based analytic model of radio galaxies

M. J. Hardcastle★

Centre for Astrophysics Research, School of Physics, Astronomy and Mathematics, University of Hertfordshire, College Lane, Hatfield AL10 9AB, UK

Accepted 2017 December 29. Received 2017 December 21; in original form 2017 October 1

ABSTRACT

I derive and discuss a simple semi-analytical model of the evolution of powerful radio galaxies which is not based on assumptions of self-similar growth, but rather implements some insights about the dynamics and energetics of these systems derived from numerical simulations, and can be applied to arbitrary pressure/density profiles of the host environment. The model can qualitatively and quantitatively reproduce the source dynamics and synchrotron light curves derived from numerical modelling. Approximate corrections for radiative and adiabatic losses allow it to predict the evolution of radio spectral index and of inverse-Compton emission both for active and 'remnant' sources after the jet has turned off. Code to implement the model is publicly available. Using a standard model with a light relativistic (electron–positron) jet, subequipartition magnetic fields, and a range of realistic group/cluster environments, I simulate populations of sources and show that the model can reproduce the range of properties of powerful radio sources as well as observed trends in the relationship between jet power and radio luminosity, and predicts their dependence on redshift and environment. I show that the distribution of source lifetimes has a significant effect on both the source length distribution and the fraction of remnant sources expected in observations, and so can in principle be constrained by observations. The remnant fraction is expected to be low even at low redshift and low observing frequency due to the rapid luminosity evolution of remnants, and to tend rapidly to zero at high redshift due to inverse-Compton losses.

Key words: galaxies: active – galaxies: jets – radio continuum: galaxies.

1 INTRODUCTION

1.1 The evolution of radio sources

A key problem in the study of radio-loud active galaxies (RLAGN) is the difficulty of inferring their dynamical state from observation. The large-scale structures we see are dynamic, not static; the size, shape, and luminosity of the lobes of RLAGN change with time. A consequence of this fact is that observational selection criteria imply biases that need to be accounted for interpretation.

The basic nature of radio source dynamics has been understood since at least Scheuer (1974), but is complex in detail. Let us first consider a source that starts in a spherically symmetric environment, at $t = 0$ and continues with a constant two-sided jet power Q (determined by the accretion system) until the jet turns off at time $t = T$. I denote the total source radio luminosity at some fixed observing frequency as L and the lobe length as R. Clearly, at $t = 0$, $L = 0$, and $R = 0$. At later times $t < T$, the growth of the lobe ($\mathrm{d}R/\mathrm{d}t$) is determined by the balance of the jet momentum flux and the internal lobe pressure, on the one hand, against the external thermal pressure and the ram pressure due to the lobe's expansion on the other. If jets are light and relativistic when they are generated, then the momentum flux of each jet is simply $Q/2c$, and the growth of the source is determined solely by the interaction with the environment with no free parameters. Unless the internal pressure in the lobe falls below the external thermal pressure, or there are catastrophic interactions with the external environment not modelled in this picture, such as high-speed bulk motions, $\mathrm{d}R/\mathrm{d}t > 0$ at all times. A source's size is thus a proxy of its age, but also its environment – without a knowledge of environment a physical size only gives a weak lower limit on age.

The radio luminosity (density) of such a source is dependent on the energy density of radiating particles and field in the lobe, and on the lobe volume, so in general initially we expect luminosity to rise with time ($\mathrm{d}L/\mathrm{d}t > 0$), though this may be masked at a given observing frequency by effects such as self-absorption for small sources. Numerical models (Hardcastle & Krause 2013, 2014) predict that the radio luminosity will then enter a phase where it is roughly constant with time (the lobe is still growing, but its pressure is falling) before starting to drop off again at late times. The peak radio luminosity for a given jet power will depend on environment (Barthel & Arnaud 1996; Hardcastle & Krause 2013). The effect of radiative losses ('spectral ageing') will start to become important

★ E-mail: m.j.hardcastle@herts.ac.uk

at a time that depends on the observing frequency, which adds an additional time-dependent declining term to the radio luminosity. So the overall expected picture is one of a relatively rapid rise, peaking at a physical size comparable to the radius at which the pressure starts to drop off rapidly with distance, followed by gradual decline. After the jet turns off, at $t > T$, the decline is expected to be more rapid as the contents of the lobes are no longer replenished with newly accelerated electrons. Analytic models agree with this general picture, though with differences in detail depending on the assumptions made (e.g. Kaiser & Best 2007).

Even without making this picture more quantitative there are some extremely important implications:

(i) Radio luminosity is a function of time, not just of jet power, and starts at zero at $t = 0$. There cannot possibly be a single conversion between radio luminosity and jet power, as hoped for in the work of, e.g. Cavagnolo et al. (2010). The best we could hope for would be a relationship between luminosity and power in the mature, large phase, which can in fact be seen in simulations (English, Hardcastle & Krause 2016). But even for those large sources, the relationship will have significant intrinsic scatter dependent on environment.

(ii) Because luminosity is dependent on age, environment and, as we will see below, particle content, selecting a sample with which to calibrate a luminosity–power relationship is fraught with bias – a relationship that applies to one group of sources may be systematically wrong for another (see Croston et al. 2018, submitted for evidence that this is in fact the case).

(iii) A flux-limited sample, which has a limit on the luminosity that can be detected at any given redshift, cannot (at fixed redshift) detect any sources at all below a certain jet power. But, more importantly, it is also biased against young and old sources. It should come as no surprise that as we go to more sensitive surveys we see fewer large, $\gtrsim$ 100-kpc scale sources and more smaller, fainter sources (Baldi, Capetti & Giovannini 2015; Hardcastle et al. 2016).

The aim of this paper is to use a simple dynamical model of radio galaxies to make some of the above statements more quantitative. Before that, however, I comment on some important observational results which need to be considered before modelling can be carried out, and motivate the development of new models by considering modelling that has been carried out in the past.

1.2 Key observations: Fanaroff–Riley class, field strength, and particle content

The discovery by Fanaroff & Riley (1974) that the structures of powerful sources was directly related to their radio luminosity is of key importance in our understanding of these objects. In particular, it demonstrates that the radio luminosity (in these objects, which of course may not be representative of the whole population) must correlate at least reasonably well with some more fundamental physical quantity which also determines the jet structure.

An entirely satisfactory physical explanation of the difference between the two types of *jet* seen in FRI and FRII sources has existed for many years – as I will argue in a moment, this is not quite the same as the difference between the two morphological classes. The key difference between the jets appears to be their speed. If we interpret the hotspots that make FRII sources edge-brightened as terminal shocks, then the jet must be supersonic in terms of its internal sound speed (for the reverse shock) or the jet head must be supersonic in terms of the sound speed in the lobes (for the forward shock). If the lobes are composed of relativistic plasma (for which see below) then this implies a relativistic bulk speed for the jet, consistent with directly obtained lower limits on jet speed from population beaming arguments (Mullin & Hardcastle 2009). On the other hand, we know from many very detailed beaming analyses (summarized by Laing & Bridle 2014) that the jets in FRI sources are relativistic on the smallest observable scales but decelerate on scales of order tens of kpc to subrelativistic, presumably subsonic speeds. This is entirely consistent with a class of model described by Bicknell (1994, 1996) in which *entrainment* plays a crucial role: all jets necessarily entrain material (from stellar winds if nothing else: Bowman, Leahy & Komissarov 1996; Wykes et al. 2015), and the final speed of a jet on escaping from the dense central regions in which it originates is determined by the original jet power Q, or more precisely its momentum flux, and the amount of material it entrains in its passage through the galaxy. Thus, the distinction between FRI and FRII jets should be related to their jet power Q and the density of their environment (perhaps by way of the stellar mass of their parent galaxy; cf. Ledlow & Owen 1996). Since momentum is conserved, it is almost impossible to evade the necessity for entrainment in order to produce the observed smooth deceleration of the jets in FRI sources; stellar mass-loss rates and populations are well known and consistent with producing deceleration from relativistic scales; and, that being the case, there is arguably no need to consider other models (e.g. of different jet opening angles, magnetic field structures, or accretion modes) unless a model based on entrainment alone can be shown to be inadequate. Moreover, there is no real reason to expect the *dynamics* of sources with these two types of jets to be fundamentally different from the simple model sketched in the previous subsection.[1]

However, it is important here to draw a distinction between the structure of the jets and the structure of the lobes, a point made very clearly by Leahy (1993). Let us for convenience label the two sorts of jet discussed above as 'slow' (FRI-type) and 'fast' (FRII-type). We can also classify the extended structures generated by jets as 'lobes' and 'plumes', where the difference is essentially one of aspect ratio; lobes are significantly fatter than plumes, and the latter often have the appearance of being a smooth continuation of the jet to large scales. 'Classical double' FRIIs of course have fast jets which feed well-defined lobes, while some of the best-studied FRI sources, such as 3C 31, have slow jets that transition seamlessly into plumes. But a lobed morphology for slow-jet sources is also extremely common, while somewhat less common, but still easily identifiable, is the population of 'wide-angle tail' (WAT) sources, which have mildly relativistic jets (Jetha et al. 2008) that often terminate in clear hotspots (Hardcastle & Sakelliou 2004) at the bases of long, extended plumes; these are classically FRI objects from their lack of edge brightening but all the evidence is that they possess 'fast', FRII-like jets. Thus, both 'slow' and 'fast' jets can have 'lobed' or 'plumed' large-scale structure. The evolution of these two types of large-scale structure is of course relevant to dynamical models, and I will return to this point below.

Another key point relating source structures to dynamical issues concerns the field strength and particle content of radio galaxies.

[1] A very prevalent error is to assume that FRI jets, which do not produce terminal shocks inside the jet or lobe material, will not drive shocks into the external medium; of course these two questions are entirely unrelated, since the momentum and energy flux of the jets are unaffected by entrainment. Observationally, some of the best examples of shocks driven by radio galaxies are in systems classed as FRIs and with characteristically FRI-like decelerating jets, such as Cen A (Kraft et al. 2003; Croston et al. 2009).

X-ray inverse-Compton observations of FRIIs (Hardcastle et al. 2002; Kataoka & Stawarz 2005; Croston, Hardcastle & Birkinshaw 2005; Hardcastle et al. 2016; Ineson et al. 2017) show conclusively, with very little room for uncertainty, that magnetic field strength B is typically a small factor below the equipartition value $B_{\rm eq}$ (where I define equipartition as with the observed radiating electrons only, i.e. $B_{\rm eq}^2/2\mu_0 = U_{\rm e}$ where $U_{\rm e}$ is the energy density in electrons). This departure from equipartition implies a departure from minimum energy, i.e. the lobes have a higher energy density, and hence pressure, for a given synchrotron emissivity than would otherwise be expected. It has also been clear for some time, but has now been demonstrated in large samples (Ineson et al. 2017) that for these FRII sources, in general, the pressure from the radiating electron population and field (constrained by inverse-Compton emission) is very close to the external thermal pressure from the cluster environment estimated at a radial distance corresponding to the mid-point of the lobes. This would be a coincidence if the internal pressure were in fact dominated by non-radiating particles, and so a plausible view is that non-radiating particles make a small (though not necessarily negligible) contribution to the internal pressure in most FRIIs. Such a conclusion greatly simplifies modelling of such sources, since it removes an ambiguity in the relationship between internal pressure and synchrotron emissivity.

On the other hand, it is well known that FRI sources generally fall well below pressure balance at equipartition. This applies not just to plumed and lobed sources with 'slow' jets (e.g. Croston et al. 2008) but also to WAT-type sources with 'fast' jets (Hardcastle et al. 2005). The favoured explanation for this is not a departure from equipartition (Croston & Hardcastle 2014) but rather that entrained thermal material is raised to high temperatures in the lobes and provides a significant contribution to the internal pressure without increasing the synchrotron emissivity. This presents a problem for modelling since the precise properties of this thermal material (temperature and equation of state) and how these depend on intrinsic source and environment are not well understood. It is clear, however, that the synchrotron emissivity of such a source will fall below what would be expected if the internal pressure were dominated by electrons. For this reason, among others, population models, which need to predict radio luminosities, tend to focus on FRII-type sources, and that is the approach in this paper as well. I emphasize, however, that the dynamical conclusions of this paper should be applicable to both types of source.

1.3 Models of source dynamics and emission

Kaiser & Alexander (1997) took an important step forward in constructing analytical models of the evolution of radio galaxies with what I will refer to as the 'self-similar model'; in this model the aspect ratio of the radio source is constant with time. With this assumption, and with the further assumption of power-law atmospheres (i.e. number density $n \propto r^{-\beta}$ with $\beta > 0$), they were able to derive analytical expressions for source growth and, later, synchrotron emission (Kaiser, Dennett-Thorpe & Alexander 1997). These models have been extremely productive of understanding, but they are only as good as their assumptions. Hardcastle & Worrall (2000) argued, based on observations of radio galaxy environments, that sources may in fact come close to pressure balance transversely at late times, while continuing to expand longitudinally: in this case, the lobe expansion is no longer self-similar (see also Luo & Sadler 2010). Numerical modelling has allowed us to investigate this scenario quantitatively (Hardcastle & Krause 2013, 2014) and confirm the qualitative picture from earlier work; at late times, a situation akin to model C of Scheuer (1974) is seen, with the central parts of the lobe being driven away from the host galaxy by the pressure of the external medium. In this case, the self-similar assumption breaks down, which affects source dynamics at late times. At the same time, the assumption of a power-law environment is not consistent with observations of clusters, which (unsurprisingly since a power-law environment is singular at $r = 0$) show a flattening of density at small radii (e.g. Croston et al. 2008) affecting the radio source dynamics at small radii or early times and invalidating the self-similar assumption by introducing at least one additional physical scale, the 'core radius', to the problem. This second feature of the self-similar models is particularly problematic, since it prevents them from being applied to modern, realistic density and pressure profiles of the group and cluster environments that powerful radio sources inhabit.

Many later versions of analytic models have followed Kaiser & Alexander (1997) in assuming self-similar expansion and/or power-law environments; this includes the work of Blundell, Rawlings & Willott (1999), Nath (2010), Mocz, Fabian & Blundell (2011), and Godfrey, Morganti & Brienza (2017). Turner & Shabala (2015) have developed a formalism which includes neither of these approximations, at the cost of significantly increased complexity, since they have to solve a large system of coupled differential equations; their model can, however, be applied to arbitrary density/pressure profiles. The objective of this paper is to develop a model that is conceptually simpler than that of Turner & Shabala (2015), in the sense that it solves a simpler system of equations, without losing the ability to describe the key physics, encoding the understanding developed from recent numerical simulations, and to use it with atmosphere models that are well matched to observations. The model is able to predict the broad-band integrated synchrotron emission and inverse-Compton emission of both active and remnant radio galaxies, and in the later sections of the paper, I present some applications to radio galaxy populations.

2 THE MODEL

2.1 Model assumptions

Rather than considering the boundary of the radio-emitting material explicitly, the model of this paper is based on a simplified description of the dynamics of the *shocked material* around the radio lobes (the 'shocked shell'), from which radio lobe properties are then inferred. I make the following assumptions:

(i) Sources have a constant (two-sided) jet power Q throughout their lifetime and start at zero size at the centre of a pristine, spherically symmetrical environment; thus the radio source is axisymmetric.

(ii) The jet is light and relativistic so that its momentum flux in one lobe is given by $Q/2c$. (It is easy to modify this assumption to deal with slower, heavier jets, and I will make use of this fact later.)

(iii) The lobes drive a shock into the external medium. The outer boundary of the shocked shell takes the form of a prolate spheroid with semi-major ('long') axis R and semi-minor axis $R_\perp$.

(iv) The unshocked external medium is isothermal (Section 3.1), i.e. it can be described with a single temperature T and therefore constant sound speed $c_{\rm s}$. It has an arbitrary, but spherically symmetrical pressure/density profile $p_{\rm ext}(r)$.

(v) *A constant fraction* ξ of the energy supplied by the jet at any given time is stored as internal energy of the relativistic lobe plasma. The remaining energy $(1 - \xi)$ is stored as additional thermal and

kinetic energy of the shocked material, between the shock front and the contact discontinuity, over and above the thermal energy that material carried across the shock. (This assumption is motivated by numerical modelling – see Hardcastle & Krause 2013; English et al. 2016 – where values of ξ between around 1/2 and 1/3 are found.) The lobe material has an adiabatic index Γ_j and the shocked material has Γ_s: in the standard models, I take $\Gamma_j = 4/3$ and $\Gamma_s = 5/3$.

(vi) The shocked shell is everywhere in (approximate) pressure balance with the lobes, as found to be the case in numerical models (Hardcastle & Krause 2014). The lobes have a single internal pressure $p = (\Gamma_j - 1)U = \xi(\Gamma_j - 1)Qt/V_L$ (i.e. there are no pressure gradients in the lobes).

(vii) The growth of the axes of the shocked shell is governed by the non-relativistic Rankine–Hugoniot conditions, in order to incorporate mass, momentum, and energy conservation at the jump between the undisturbed and swept-up gas. In the case of transverse expansion, only the internal pressure of the shocked gas drives the expansion. In the case of longitudinal expansion, the ram pressure of the jet, distributed over the cross-sectional area of the lobes, is also relevant.

(viii) The lobe long axis (the axis of longitudinal growth as in the previous point) is close to the long axis of the shocked shell at all times, again as found in numerical models, so that the length of one lobe is approximately R.

(ix) Radiative losses are negligible (in terms of their effects on the energetics) at all times – I test this assumption below.

Assumption (vii) gives us the following differential equations for the expansion of the shocked shell:

$$\frac{\mathrm{d}R}{\mathrm{d}t} = c_s\sqrt{\frac{(\Gamma_s + 1)(p_R/p_{ext}(R)) - (1 - \Gamma_s)}{2\Gamma_s}} \quad (1)$$

$$\frac{\mathrm{d}R_\perp}{\mathrm{d}t} = c_s\sqrt{\frac{(\Gamma_s + 1)(p_{R_\perp}/p_{ext}(R_\perp)) - (1 - \Gamma_s)}{2\Gamma_s}} \quad (2)$$

where the pressures to use are given [assumptions (ii) and (v)] by

$$p_R = \frac{\epsilon QR}{2cV_L} + \frac{(\Gamma_j - 1)\xi Qt}{V_L} \quad (3)$$

$$p_{R_\perp} = \frac{(\Gamma_j - 1)\xi Qt}{V_L} \quad (4)$$

The second of these is the true internal pressure of the lobe, which by assumption (vi) is the same as the pressure of the shocked material: the difference between the two pressures arises from assumption (vii). I estimate the cross-sectional area of the lobe tip as $V_L/\epsilon R$, by assumption (viii). ϵ is a geometrical factor reflecting the fact that the lobe is not cylindrical, so that the jet momentum flux is not spread over the whole cross-section of the lobe: I set $\epsilon = 4$ in what follows based on comparison with simulations. Note here that the internal pressure is almost always higher than the external pressure, so that the expansion speed $\mathrm{d}R/\mathrm{d}t$ in both directions is higher than the sound speed c_s. In some unusual cases, the pressure of the shocked material can fall below the internal pressure in the perpendicular direction (e.g. when the source is expanding very fast in the longitudinal direction). This is unphysical, but in this case, I force the expansion speed to equal the sound speed, i.e. the correct speed for the growth of the shell of gas that can possibly be influenced by the radio galaxy, and the underpressuring is usually a transient event.

The volume of the lobes V_L is given, as a consequence of assumptions (v) and (vi), by

$$\frac{V_L}{V_T} = \frac{(\Gamma_j - 1)\xi Qt}{[\xi\Gamma_j + (1 - \xi)\Gamma_s - 1]Qt + NkT - (\Gamma_s - 1)\mu Nv^2/2} \quad (5)$$

where V_T is the total volume inside the shock front [assumption (iii)]:

$$V_T = \frac{4}{3}\pi R R_\perp^2 \quad (6)$$

μ is the mass per particle in the external medium, v is a measure of the lobe expansion speed (see below), and N is the total number of particles of the external medium that have been swept up by the expanding shock front, i.e.

$$N = \int_{V_T} n\mathrm{d}V \quad (7)$$

where the integral is taken over the spheroidal volume and is hence a function of R and $R_\perp$. (Notice that the lobe occupies a constant fraction $\xi/(2 - \xi)$ of the region behind the shock front until the swept-up thermal energy becomes comparable to the energy supplied by the jet.)

These coupled differential equations can be solved numerically for R and $R_\perp$. A numerical integral is of course necessary to compute N in general, and some initial conditions need to be supplied – I take $R, R_\perp = ct_0$ at some small initial time t_0. The initial expansion would be expected to be relativistic, but this phase lasts a comparatively short time, and rather than try to model it accurately we simply cap the lobe expansion speed at c and use non-relativistic physics. I have verified that using the more complex expressions provided by Gallant (2002) for a strong relativistic shock at early times makes no significant change to the late-time behaviour. In addition, we need to make a self-consistent correction for the kinetic energy of the shocked material, the term in v^2 in equation (5), since equations (1) and (2) depend on this term through equations (3) and (4). This is implemented, approximately, by iteratively computing V_L and the expansion speed and solving using a bisection method for $v^2 = \sqrt{R_\perp(\mathrm{d}R/\mathrm{d}t)^2 + R(\mathrm{d}R_\perp/\mathrm{d}t)^2]/(R + R_\perp)}$; the weighted mean of the velocities here is intended to take account of the shape of the expanding shock front.

This model has some strengths and weaknesses compared to others which it is worth discussing in detail. Compared to e.g. the analytic models of Kaiser & Alexander (1997), or the many others discussed above that use power-law atmospheres, it has the advantage that it can deal with any external pressure/density profile, including realistic ones. It also allows for the evolution of the shock aspect ratio with time by modelling the transverse and longitudinal expansion separately. I model both the transition between ram-pressure and thermal-pressure-dominated expansion (equation 3) and also between the situation where the energy advected across the shock front is negligible and where it is not (equation 5). Unlike the model of Turner & Shabala (2015), some of the assumptions break down if the expansion speeds become trans-sonic – since then the effect of the radio source is not confined to a shocked shell – and, in common with all models, it has difficulties if there is substantial entrainment of thermal material into the lobes themselves, which would change their equation of state and also affect the radio luminosity calculations of the following section. These two limitations mean that it is most applicable to powerful sources; but this is still adequate for the purposes of the remainder of this paper.

2.2 Radio luminosity

Radio luminosity is computed in the manner applied by Hardcastle & Krause (2013) to numerical models. Suppose we know that the magnetic field energy density is always some constant fraction of the electron energy density:

$$\zeta U_\mathrm{e} = U_\mathrm{B} = \frac{B^2}{2\mu_0} \tag{8}$$

where ζ describes the energetic departure from equipartition between field and radiating electrons, and it is reasonable to assume $\zeta < 1$ (see Section 1.2). I further assume that the energy density in non-radiating, relativistic particles (e.g. protons) is given by $U_\mathrm{NR} = \kappa U_\mathrm{e}$. For a fully tangled field, the pressure in the radio source, p, can be related to the energy densities in electrons and field.

$$p = \frac{U_\mathrm{e} + U_\mathrm{B} + U_\mathrm{NR}}{3} = \frac{(1 + \zeta + \kappa)U_\mathrm{e}}{3} \tag{9}$$

or, equivalently,

$$B = \sqrt{2\mu_0 \frac{3p\zeta}{1 + \zeta + \kappa}} \tag{10}$$

Now suppose that the electron energy distribution is a power law in energy with electron energy index q, i.e.

$$U_\mathrm{e} = \int_{E_\mathrm{min}}^{E_\mathrm{max}} N_0 E^{1-q} \mathrm{d}E = N_0 I \tag{11}$$

where

$$I = \begin{cases} \ln(E_\mathrm{max}/E_\mathrm{min}) & q = 2 \\ \frac{1}{2-q}\left[E_\mathrm{max}^{(2-q)} - E_\mathrm{min}^{(2-q)}\right] & q \neq 2 \end{cases} \tag{12}$$

q here would be expected to be set by particle acceleration processes: for strong shocks, we might expect $q \sim 2$, but the particle acceleration physics is not part of the model, so q is a parameter that should be set by the user. I is only weakly dependent on E_min and E_max for plausible values of q. I use values corresponding to $\gamma_\mathrm{min} = 10$ and $\gamma_\mathrm{max} = 10^6$ in what follows. The choice of $\gamma_\mathrm{min} = 10$, which has been used in much previous work, is driven by the suggestion of low-energy cut-offs around Lorentz factors of a few hundred in hotspots (see e.g. Hardcastle 2004, for a compilation) together with some assumptions about adiabatic expansion from the scale of the hotspots and the lobes, although it now seems plausible that the detailed hotspot energy spectrum is not consistent with a sharp cut-off (McKean et al. 2016). The difference over the range $1 < \gamma_\mathrm{min} < 100$ is negligible compared to other uncertainties for $q \approx 2$.

It can be shown (e.g. Longair 2010) that for a power-law distribution of electrons, the volume spectral emissivity of synchrotron radiation is given by

$$J(\nu) = C N_0 \nu^{-\frac{(q-1)}{2}} B^{\frac{(q+1)}{2}} \tag{13}$$

where

$$C = c(q)\frac{e^3}{\epsilon_0 c m_\mathrm{e}}\left(\frac{m_\mathrm{e}^3 c^4}{e}\right)^{-(q-1)/2} \tag{14}$$

($c(q)$ here is a dimensionless constant, of order 0.05 for plausible values of q – see Longair 2010 for details.)

Therefore (since $N_0 = U_\mathrm{e}/I$), the total radio luminosity per unit frequency can be written

$$L_\mathrm{radio} = J(\nu)V = \frac{C}{I}\frac{E_\mathrm{lobe}}{1 + \zeta + \kappa}\nu^{-\frac{(q-1)}{2}} B^{\frac{(q+1)}{2}} \tag{15}$$

where B is given by equation (10) applied to the internal pressure in the lobe (equation 4), and $E_\mathrm{lobe} = \xi Q t$.

One can see that a substantial energy density in non-radiating particles ($\kappa \gtrsim 1$) reduces both B (equation 10) and the normalization of L_radio. As noted above, for FRI sources there is evidence that non-radiating particles entrained from the environment in the process of jet deceleration have a significant role, and in that case, the radio luminosity will be lower for a given jet power and lobe volume. [Although, on the face of it, equation (15) is independent of lobe volume, a volume dependence enters through the dependence on B, which depends on energy density.] The standard assumption in the rest of the paper will be that, for the FRII sources I aim to model, $\kappa = 0$.

2.3 Loss processes

It is very important to take account of the effects of radiative and adiabatic losses on the observed synchrotron radiation. Since we are assuming that Q is constant [assumption (i) above], we can make the related (though not identical) assumption that the supply of high-energy particles in power-law form is constant with time, as done by Kaiser et al. (1997) and papers following that formalism. Then, the true electron energy spectrum of the lobes at time t is the integral

$$N(E) = \int_0^t N_\mathrm{aged}(E, t_\mathrm{inj}, B_\mathrm{eff})\mathrm{d}t_\mathrm{inj} \tag{16}$$

where N_aged is the suitably normalized electron energy spectrum of a population of electrons injected at time t and B_eff is the effective magnetic field strength that has aged those electrons, taking into account the time variation of B and losses to inverse-Compton scattering of the cosmic microwave background (CMB) – that is, B_eff is itself a time average of B^2 and B_CMB^2 between t_inj and t. The synchrotron spectrum of that population can then be calculated using the current value of B and used to derive a correction for the pure power-law spectrum of equation (11). For these purposes, I use simple Jaffe & Perola (1973) aged spectra[2] and compute the synchrotron spectrum of aged populations at a finite set of discrete times in order to approximate the emission from the electron population of equation (16), using a version of the code of Hardcastle, Birkinshaw & Worrall (1998). Note that I am assuming here that each element of the electron population contributes equally to the synchrotron emissivity: this may not be the case if, e.g. there is magnetic field structure in the lobe.

Adiabatic losses may be represented as a further correction to the radiative loss factor. Adiabatic expansion from volume V_0 to volume V_1 reduces the energies of all electrons in the volume: $E \propto (V_1/V_0)^{-1/3}$. As the characteristic electron energy for aged electrons goes as t^{-1}, we can correct approximately for adiabatic effects on the spectrum by increasing the effective age of a population by a factor of the cube root of the ratio of the volume of the lobes at injection to the currently observed volume, as if the particle population had first aged and then abruptly expanded to their current volume. This is only an approximation, since in reality the lobe expansion and the radiative losses occur in parallel, but the correction turns out to

[2] As discussed by Hardcastle (2013), alternatives that do not involve pitch angle scattering of the electrons, such as the widely used Kardashev–Pacholczyk models (Kardashev 1962; Pacholczyk 1970) are not realistic; we would obtain similar results by using the more physically realistic Tribble (1991) models, but at significantly increased computational cost.

be a small one in any case. The effects of adiabatic losses on the energy density in the lobes are assumed to be taken account of by assumption (v).

2.4 Inverse-Compton emission

Inverse-Compton emission due to scattering of the CMB, the other main detected loss process of radio galaxies, can be modelled in a very similar way to synchrotron emission; to determine the inverse-Compton emissivity I integrate over the full electron and photon distribution with a suitable kernel in the manner described by Hardcastle et al. (1998). With a simple power-law assumption for the electron energy spectrum, this process gives an inverse-Compton luminosity that increases linearly with time for $t < T$ and is independent of environment, because volume emissivity is proportional to the normalization of the electron spectrum, and

$$N_0 V \propto \frac{\xi Q t}{1 + \zeta + \kappa} \tag{17}$$

With corrections for loss and adiabatic expansions as described in the previous subsection, it is possible for electrons of the required energy for inverse-Compton scattering to a particular energy (e.g. $\gamma \sim 10^3$ to scatter the CMB into the soft X-ray at $z = 0$) to be removed, introducing an environment dependence of the inverse-Compton luminosity.

I do not consider nuclear inverse-Compton or synchrotron self-Compton processes in this paper either as a radiative loss term or as a source of observable photons. The former would add a dependence on the accretion state of the AGN generating the jet, which complicates the picture significantly, and is in any case only important for small sources because of the $1/r^2$ dependence of the photon energy density. The latter is never dominant over synchrotron emission.

3 MODEL RESULTS

3.1 Realistic model atmospheres

I select two model atmospheres in the current paper for the purposes of testing.

The first is the widely used isothermal beta model (Cavaliere & Fusco-Femiano 1978), where we have

$$p = p_0 \left[1 + \left(\frac{r}{r_c}\right)^2\right]^{-3\beta/2} \tag{18}$$

and $n = p/kT$. The smoothness and simplicity of this model makes it a quick and easy basis for testing and results that use it can also be directly compared with the numerical models of HK13 and HK14. However, it is not particularly well motivated either by theory or observation, and has four free parameters (p_0, kT, r_c, and β) which do not map in a particularly obvious way on to the richness of a group or cluster (other than in the obvious qualitative sense that larger p_0, kT, or r_c imply more gas).

The second is the so-called universal pressure profile of Arnaud et al. (2010). This is derived from the observed pressure profiles of a well-studied sample of clusters, and has the great advantage that it is calibrated in terms of a single free parameter, the total mass of the system, M_{500} (the total gravitating mass within the radius R_{500} corresponding to a density contrast of 500 times the critical density of the Universe) – a given M_{500} uniquely specifies the pressure profile. Although this relationship was calibrated for clusters with

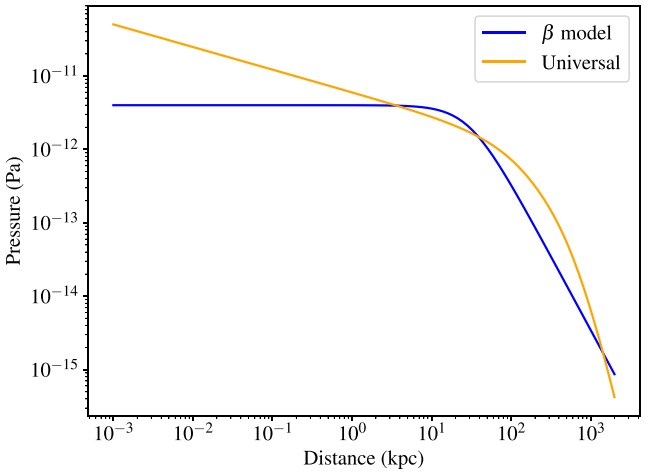

Figure 1. Pressure profiles for a representative β model and Arnaud et al. (2010) universal pressure profile, as described in the text.

$10^{14} < M/M_\odot < 10^{15}$, Sun et al. (2011) have shown that it can be extended to groups, and therefore it applies across the range of environments known for powerful radio galaxies. I implement the universal pressure profile using the prescription in section 5 of Arnaud et al. (2010), and then assume an isothermal temperature profile with kT from the M_{500}–kT relation of Arnaud, Pointecouteau & Pratt (2005) in order to convert to density for model testing (incorporating a temperature profile would be trivial in the context of the modelling but is not necessary at this point).

Fig. 1 shows a comparison between a universal pressure profile with $M_{500} = 10^{14} M_\odot$ and a β model with $p_0 = 4 \times 10^{-12}$ Pa, $r_c = 30$ kpc, $\beta = 2/3$, and $kT = 2.3$ keV, both intended to represent a poor cluster environment not uncommon for radio galaxies (Ineson et al. 2015). It can be seen that the most important difference is in the pressure (therefore density) at small radii, <1 kpc, but there are non-negligible differences at large radii too.

3.2 Simple source dynamics

In this section, I use the two model atmospheres from Section 3.1 to present some basic results of the modelling. I model the propagation of a light relativistic jet with $Q = 2 \times 10^{39}$ W into both atmospheres and solve for times in the range 0–300 Myr. The power is chosen to match the intermediate power used in the numerical simulations of English et al. (2016), and I set $\xi = 0.4$, also matching their results. Fig. 2 shows some key dynamical quantities from the results.

The top left plot of Fig. 2 shows the source expansion with time: the basic features of this plot are common to all modelled sources. Expansion is originally relativistic but transitions to subrelativistic lobe advance speeds on short time-scales, ∼1000 yr in this case. It is important to remember that the model is not accurate when the expansion speed is relativistic. There then follows a phase of decelerating expansion (compare the bottom left plot, which shows the Mach number of expansion): in the β-model environment, where the density profile is essentially flat on these scales, the lobe growth has the expected $R \propto t^{3/5}$ slope (Kaiser & Alexander 1997). The lobe advance speed then changes (flattening off in the β-model case or accelerating in the universal pressure profile case) when the front of the lobe starts probing the steep pressure gradient on scales of ∼100 kpc. It is also worth noting the comparatively slow growth of these model sources – in 300 Myr, the source has grown only to Mpc scales, implying an average growth speed of ∼0.01c. Although the

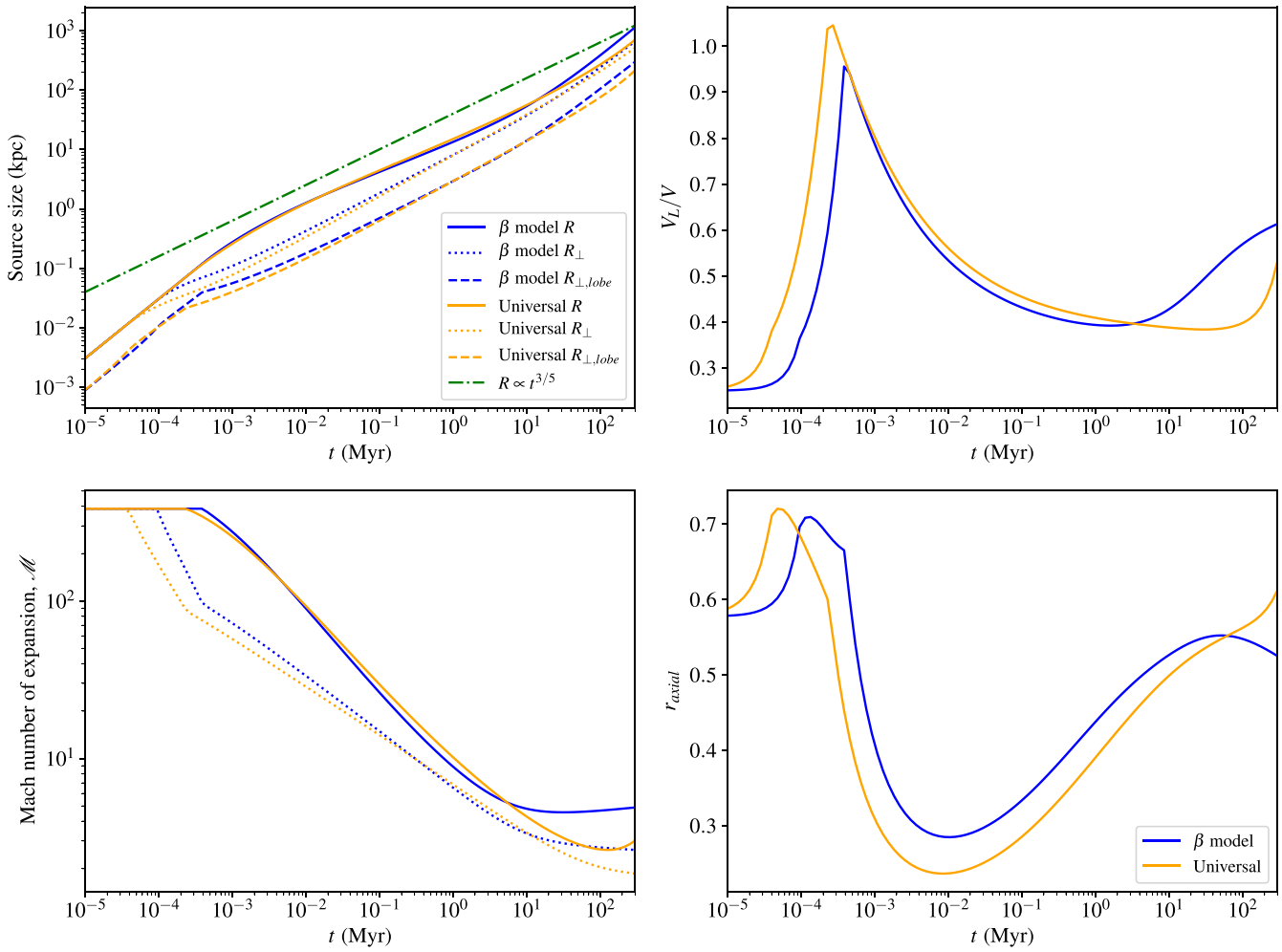

Figure 2. Dynamical quantities for a jet of $Q = 2 \times 10^{39}$ W in two poor cluster environments as described in the text. Top left: source length R, perpendicular source radius $R_\perp$, and perpendicular lobe radius $R_{\perp,\,\mathrm{lobe}}$: an arbitrarily normalized line of $R \propto t^{3/5}$ is also shown. Top right: lobe volume as a function of total volume, V_L/V. Bottom left: Mach number of the longitudinal and perpendicular advances of the shocked region. Bottom right: the axial ratio of the radio source $2R_{\perp,\,\mathrm{lobe}}/R$.

figure clearly depends on the environment and jet power, slow jet head advance speeds are a feature of light jets such as those used here.

The expansion is clearly not self-similar – note both the modest changes in the fraction of the volume occupied by the lobe in the top right plot and the much larger changes in the source axial ratio in the bottom right. The axial ratio behaviour we see here can qualitatively be understood in terms of the different density regimes and the evolution of pressure in the lobes, which lead to different expansion speeds at different times. At very early times, the lobes are expanding relativistically in all directions, and so we see almost spherical lobes with large axial ratios. Once this phase is over, the lobes grow linearly much faster than they do transversely because the ram-pressure term in equation (3) dominates over internal pressure: however, as the source expands the ram-pressure term becomes less important, and so at later times, the transverse and longitudinal expansion speeds become more similar and consequently (integrated over time) the lobe linear and transverse sizes become more similar. At the very latest times shown in the figure, the tips of the lobe start to probe the very steep downwards density/pressure gradient in the outskirts of the cluster and consequently the longitudinal expansion starts to accelerate, while the transverse expansion continues to decelerate: this leads to a decrease in the axial ratio again.

3.3 Comparison with simulations

For a direct comparison with simulations, I model jets in the set of environments used in the numerical models of HK13, i.e. β models with $kT = 2$ keV, $p_0 = 10^{-11}$ Pa, $\beta = [0.55, 0.75, 0.90]$, and $r_\mathrm{c} = [20, 30, 40] \times 2.1$ kpc. I omit the unrealistically flat $\beta = 0.35$ models for simplicity and use a two-sided jet power of 2×10^{38} W. In order to match HK13's jet conditions, I adjust the jet momentum flux so that it is appropriate for an $\mathcal{M} = 25$ jet of this power (a 'heavy jet'), and set the adiabatic index of the jet material Γ_j to 5/3.

Fig. 3 shows comparisons between (left-hand panel) the lobe lengths and (right-hand panel) the volume of the shocked region, in simulations and analytic models. It can be seen that the analytical models agree well with the simulations at late times on the expected lobe lengths: at early times, the simulations are affected by the pixel size in the simulation and by problems coupling the boundary-condition jet to the ambient medium. The analytical models show the same late-time qualitative trends and quantitatively agree to within ∼20 per cent for most simulations. It is important to note here

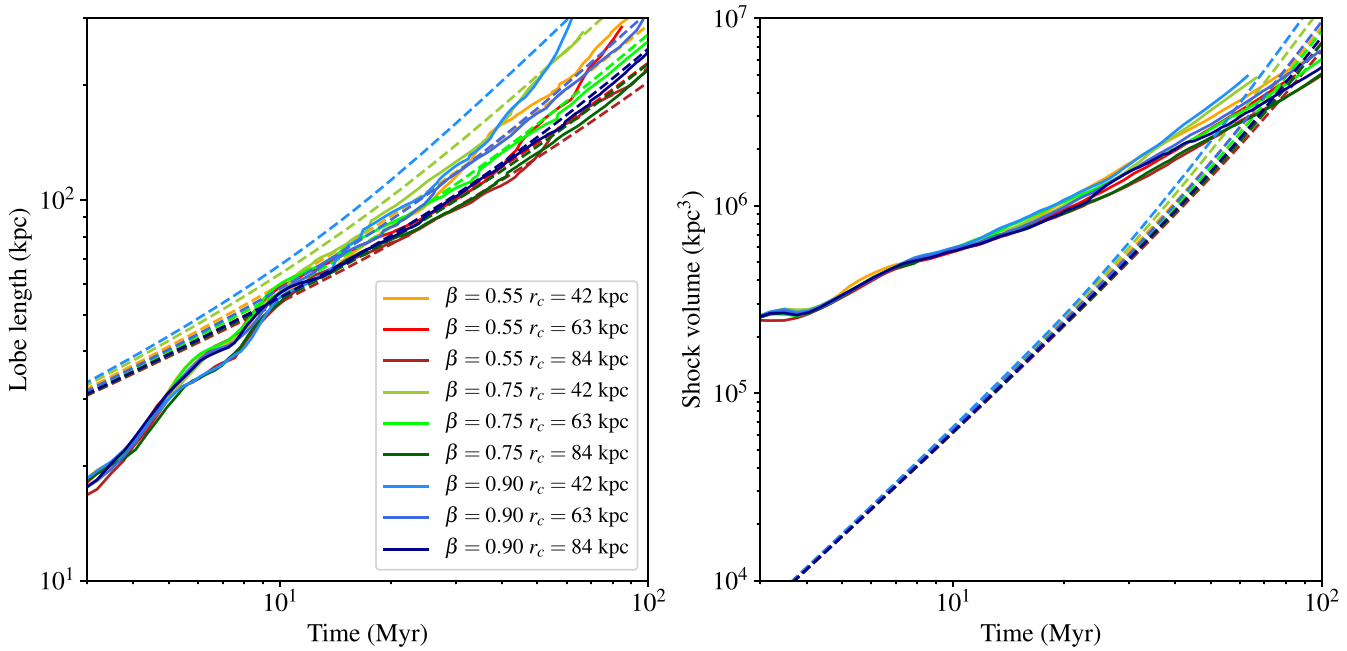

Figure 3. Analytic models compared with the HK13 2D heavy jet numerical models. Left: lobe/shocked region length. Right: shocked region volume. Solid lines show the hydrodynamical simulations and dotted lines show the analytical models.

that for these heavy jets, the jet momentum flux is still important in driving the forward expansion of the lobes at late times, so the agreement here is not particularly surprising, particularly as the parameter ϵ has been chosen to produce general agreement with simulation results.

The shock volumes in the analytical and numerical models also agree reasonably well at late times. The numerical model volumes are unrealistically high in volume at early times (due to resolution effects and to the use of a boundary-condition jet, the shock in the numerical models effectively has non-zero size at $t = 0$), but at later times, they are close to consistent, though with a different gradient. The numerical models do predict smaller shocks at the very latest times. Part of this may be due to the effect of the lobes pinching off in their central regions and ceasing to drive transverse expansion, an important feature of the numerical models which the analytical models do not include. This coincides with a transition to trans-sonic or subsonic expansion in the analytical models, and I have already noted that this regime is unlikely to be modelled well. As a consequence, the lobes themselves are larger and (since by construction the total energies in the two regions have a constant ratio) the pressure in the lobes and shocked regions is smaller than in the numerical models at a given late time.

3.4 Synchrotron emission and losses

The top panel of Fig. 4 shows the synchrotron emission as a function of time expected for the universal pressure profile, $Q = 2 \times 10^{39}$ W system described in Section 3.2 for various frequencies commonly used in radio astronomy. Also plotted is the integrated spectral index α (defined in the sense that $S \propto \nu^{-\alpha}$) for each adjacent pair of spectra. I set $q = 2.1$, corresponding to an 'injection index' $\alpha = 0.55$ which would be expected in models of particle acceleration at strong shocks, and assume $z = 0$ and $\zeta = 0.1$, the latter based on the results of Croston et al. (2005) – unlike Blundell et al. (1999) I do not try to model any dependence of the injection index on jet power. I also plot the 150-MHz luminosity uncorrected for any spectral age or adiabatic loss effects, i.e. derived purely as discussed in Section 2.2.

This plot has several important features. First, we can see that as seen in numerical modelling (HK13, HK14, and E16), but unlike what is the case in analytical models based on the assumption of a power-law atmosphere (Kaiser et al. 1997; Mocz et al. 2011), the synchrotron luminosity starts low, rises to a peak, and then falls off again. (The peak in luminosity at very early times, $t \lesssim 10$ yr, comes from the phase of the source's life in which its expansion speed is limited to the speed of light: given the approximations used in this regime it should probably not be taken too seriously.) The evolution of the radio luminosity seen in these plots between times of $\sim 10^{-2}$ and 10^2 Myr is generally to be expected from any model with a pressure/density profile which starts relatively flat and then steepens, together with an equipartition-type assumption. (Note that the luminosity at very early times would be affected by synchrotron self-absorption, which is not modelled here.) The fall in synchrotron luminosity at late times (which starts to become obvious when the source size approaches the linear size at which the pressure gradient slope changes) is made more prominent, but *not* caused, by the effects of radiative and adiabatic losses, as can be seen from the uncorrected light curve.

Secondly, we see different evolution of the light curves at different frequencies. The integrated spectrum of the source is expected to be curved downwards at all frequencies (here, unlike in real sources, there are no confusing effects of beamed flat-spectrum jets or self-absorbed cores), but the curvature changes with time. The low-frequency integrated spectral index of the source is steeper than the injection index at effectively all times (again, it is important to note that the intrinsic spectral index at very early times would be rendered unobservable by self-absorption). Note also that, self-absorption effects aside, the low-frequency light curve is the one that changes *most* with time – as expected since it is affected most strongly by the evolutionary history of the source, which tends to be erased by radiative losses at high frequencies. In reality, of course,

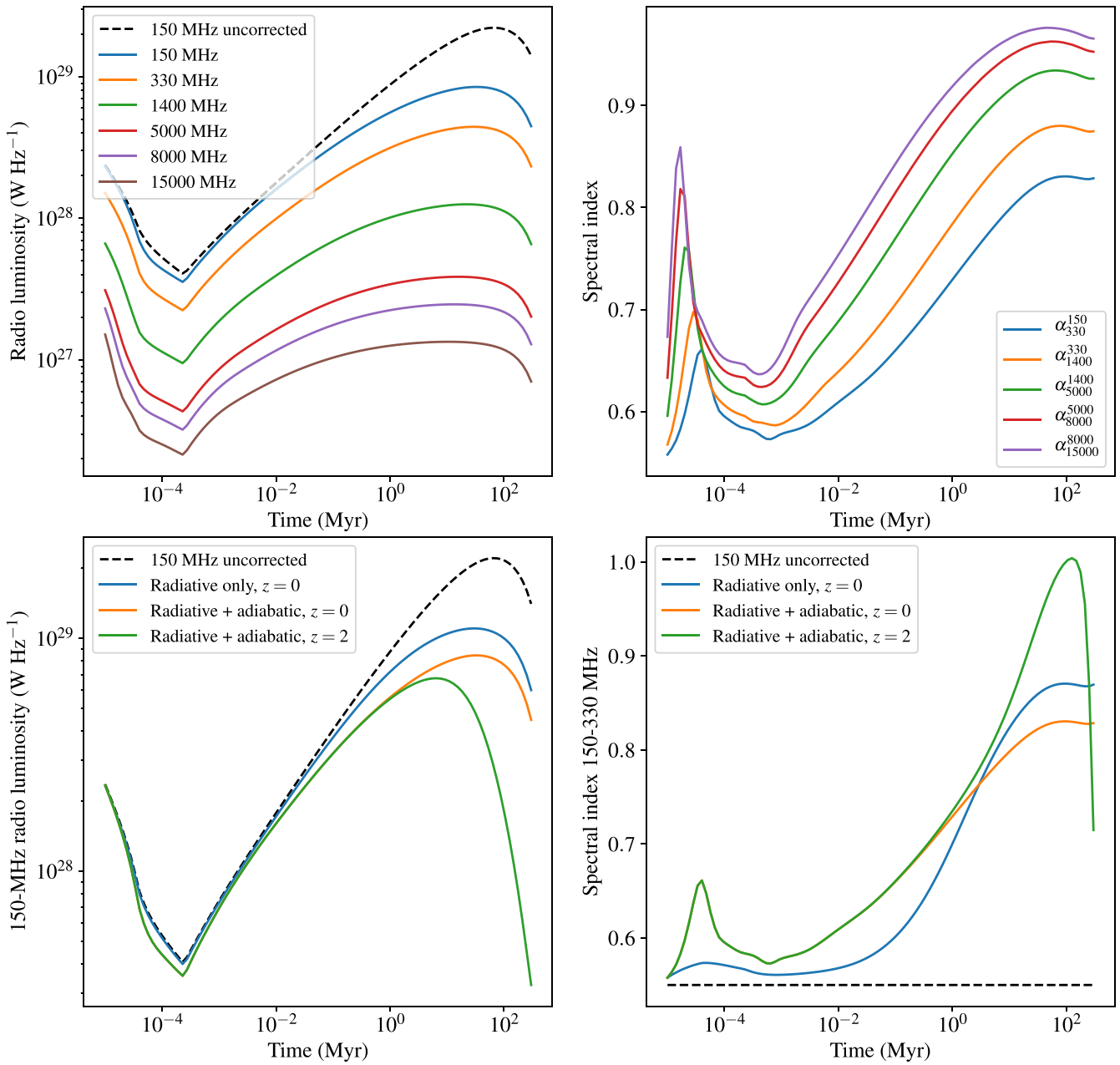

Figure 4. Synchrotron emission as a function of time for a universal pressure profile with $M_{500} = 10^{14} M_{\odot}$ and a light jet with $Q = 2 \times 10^{39}$ W. Top two panels: coloured lines show (left) radio luminosity at different frequencies and (right) spectral index between adjacent pairs of frequencies at $z = 0$ and with corrections for spectral ageing and adiabatic losses, with the uncorrected 150-MHz emission luminosity plotted for reference. Bottom two panels: the radio luminosity at 150 MHz, and the spectral index between 150 and 330 MHz, on different assumptions about the redshift and the inclusion of the adiabatic expansion correction.

high-frequency light curves will be affected by beaming and by transient features such as hotspots which are not modelled here. Another important feature of the models is that spectral index does not steepen monotonically with time – at late times, after the onset of rapid expansion of the source, we actually see a flattening of the spectral index (which is likely due to the fact that at late times very old material has an increasingly negligible effect on the integrated spectrum). At no point in the source evolution is the spectrum over this range modelled well as a broken power law or 'continuous injection (CI)' model (Kardashev 1962), consistent with some of the sources discussed by Harwood (2017). The deviation from the CI expectation comes about because the loss rates (both to adiabatic and radiative losses) are not constant with time in the source modelled here, and will be reduced for large, old sources where inverse-Compton radiative losses dominate, which may help to explain why Harwood (2017) found some sources to be reasonably well described by the CI model. Of course, it is important to bear in mind that the detailed spectral index behaviour depends crucially on the assumption that the magnetic field energy density is a constant fraction of the total, something that we do not know to be true for real radio sources, and on the assumed value of the injection index q and the energy density to electron energy ratio parameter ζ.

The normalization of the radio luminosity that is found here is very consistent with the numerical results of E16 for light jets of the same power, which do not take into account radiative losses but which of course make similar observationally based assumptions about the injection index and magnetic field to electron energy density ratios. More importantly, it is consistent with the observed jet power/radio luminosity relation given by Ineson et al. (2017), bearing in mind that the sources in the latter paper, by selection, tend to be large, powerful objects which will be close to the peak of their light curves: I return to this point below (Section 4.4).

To make the effects of the different assumptions clear, the bottom panel of Fig. 4 shows the 150-MHz luminosity, and 150–330 MHz (rest-frame) spectral index, for four different combinations of assumptions: no corrections; $z = 0$ spectral ageing only; $z = 0$ spectral ageing and adiabatic losses (as in the top panel), and $z = 2$ spectral ageing and adiabatic losses. The comparison of the first three of these demonstrates, as noted in Section 2.3, that the effect of the approximate correction that I make for adiabatic losses is relatively small, though not negligible, on both the total luminosity and integrated spectral index; the effect of spectral ageing alone is more significant. By contrast, comparing the $z = 0$ and 2 curves, we can see that the effects of going to high redshift (so increasing losses to the CMB) are very significant, as noted by Kaiser et al. (1997). These losses start to become important when the energy densities in magnetic field and CMB photons are comparable, which for the modelled source occurs after only a few Myr at $z = 2$. A very striking effect is seen in the spectral index plot, where we see that the high-z source does indeed have a steeper spectrum than at low z over some of its evolution, but at later times has a flatter spectrum. This is because inverse-Compton losses have removed almost all of the aged electrons, leaving only flat-spectrum material that has recently been injected. The well-known association between higher z and steeper spectrum (if it exists at all and is not just a luminosity–α relation) might therefore be a selection effect in flux-limited samples.

3.5 Remnant sources

It is clear that the model above can relatively easily be modified to deal with non-constant jet power Q, e.g. by replacing terms in Qt by an integral of Q over time. In general, we know too little about variations in Q with time in real sources to make this a worthwhile exercise. However, remnant sources, where the jet turns off in the course of the source's evolution, are an important special case which is easy to implement. Here effectively, we need to consider

$$Q = \begin{cases} Q_0 & 0 < t < T \\ 0 & t \geq T \end{cases} \tag{19}$$

The ram pressure of the jet also drops to zero at $t > T$. If we retain all the other assumptions, then the dynamics alter, we have

$$p_{\rm R} = p_{\rm R\perp} = \xi(\Gamma_{\rm j} - 1)QT/V_{\rm L} \tag{20}$$

for $t > T$. Similar changes need to be made to deal with the term for the internal energy of the lobes ξQt wherever else it appears, e.g. in the computation of radio luminosity. Finally, the radiative loss code needs to be modified to take account of the fact that particle acceleration will cease, i.e. no new particles will be injected for $t > T$. Although it seems likely that in reality others of the model assumptions will break down (e.g. the constancy of ξ as the source expands) these modifications are sufficient to give an impression of the expected evolution of a remnant source.

To examine remnant evolution, I take the same case of a powerful ($Q = 2 \times 10^{39}$ W) jet in a uniform pressure profile with $M = 10^{14}\,{\rm M}_\odot$ at $z = 0$, but now allow the jet to switch off after 100 Myr. The results are shown in Fig. 5, which can be compared directly to Fig. 4, although I now focus on the time evolution after 1 Myr. One can see a very rapid drop in the synchrotron luminosity of the source at all frequencies immediately after the jet is disconnected, as also seen in the quite different models of Godfrey et al. (2017). Two effects contribute to this drop. First, the dynamics of the source change, as the drop in lobe pressure due to the continued expansion at the lobe tip is no longer counteracted by the energy supply: this leads to a drop in B as a function of time. Secondly, and dominantly as can be seen by comparing the corrected and uncorrected light curves, radiative and adiabatic losses are no longer offset by a continued injection of young particles. The effect is an almost instantaneous disappearance of the high-frequency emission. Even low-frequency emission drops by an order of magnitude over 100 Myr. Loss effects would of course be much more significant at higher redshift where inverse-Compton losses dominate (see Fig. 6 for an example of this). The time-scales for a significant drop in luminosity will depend on the jet power and environment, but it seems clear that this rapid fading of the lobes can contribute to the small fraction of remnant radio galaxies seen at low frequencies (for recent constraints on this fraction see Brienza et al. 2017; Godfrey et al. 2017; Mahatma et al. 2018). I discuss this point further below, Section 4.3.

3.6 Inverse-Compton light curves

As noted above, uncorrected inverse-Compton light curves are linear with time until the jet turns off. Correction factors for expansion and radiative losses are expected to be non-negligible, though, because electrons injected at early times will only contribute at very low energies. After the jet switches off, the inverse-Compton emission will decline. Fig. 6 shows example inverse-Compton light curves for the remnant source of the previous section, with loss and adiabatic corrections applied, for $z = 0$ and 2. In both cases, we see that the decline of inverse-Compton emission with time is much slower than the synchrotron light curve, as expected since the synchrotron emission is due to higher energy electrons. Both qualitatively and quantitatively, these curves are very similar to those found by Mocz et al. (2011) – compare in particular their fig. 3 with the right-hand panel of Fig. 6 – apart from the unrealistically high synchrotron emission at early times in their figure, a result of their assumptions about environment. This supports their prediction of inverse-Compton 'ghosts' associated with the remnants of powerful sources, particularly at low z where the decline in inverse-Compton emission is very slow. One might expect to find these associated with steep-spectrum radio remnants which could be identified in e.g. surveys with the LOw-Frequency ARray (LOFAR) surveys. Of course, the X-ray surface brightness of these structures will be low at low redshift, where their angular size is large, and distinguishing their emission from thermal emission from the environment may prove challenging.

3.7 Integrated losses and self-consistency

I finally carried out a consistency check of assumption (ix), i.e. that the integrated losses may be neglected compared to the input jet power in determining the dynamics. To do this, it is necessary to integrate the standard equations for total single-electron synchrotron

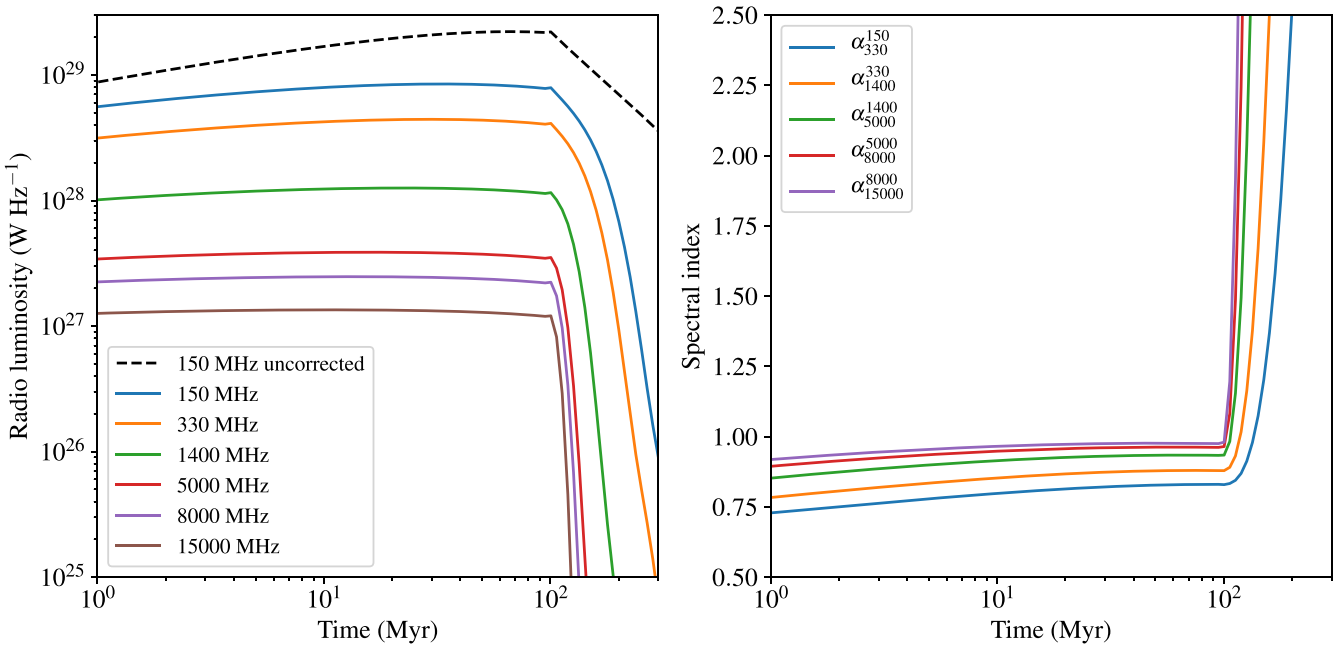

Figure 5. Synchrotron emission as a function of time for a universal pressure profile with $M_{500} = 10^{14} M_\odot$ and a light jet with $Q = 2 \times 10^{39}$ W at $z = 0$, switched off after 100 Myr and enabled to evolve for a further 200 Myr. Lines as in top two panels of Fig. 4, but note the different scales on the axes.

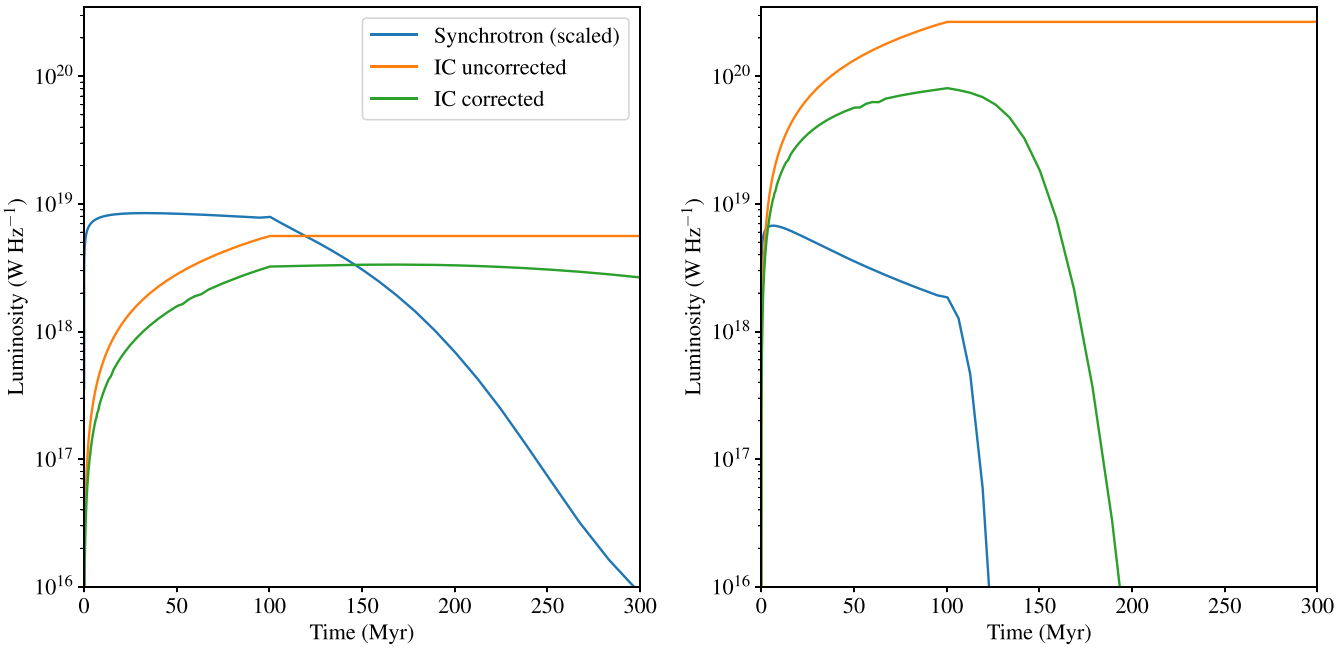

Figure 6. Inverse-Compton and synchrotron emission as a function of time for the remnant source of Fig. 5. Here, I use a linear time-scale to emphasize the decay phase. Synchrotron emission is calculated at *rest-frame* 150 MHz and inverse-Compton at rest-frame 1 keV (2.4×10^{17} Hz). The synchrotron luminosity has been scaled down by a factor 10^{10}. Left: $z = 0$. Right: $z = 2$.

and inverse-Compton losses over the electron distribution, e.g. for synchrotron we have

$$P = \int_{E_{\rm min}}^{E_{\rm max}} \frac{4}{3} \sigma_{\rm T} \frac{B^2}{2\mu_0} c \left(\frac{E}{mc^2} \right)^2 N(E) {\rm d}E \qquad (21)$$

and a similar result holds for inverse-Compton where the energy density in photons is substituted for the energy density in the field. Here, it is absolutely necessary to apply a correction for losses to the electron spectrum in the manner described in Section 2.3, since assuming a power-law spectrum extending up to high energies greatly overestimates the power P. I also roughly estimated the thermal bremsstrahlung emissivity of the shocked shell by considering its mean number density, volume, and temperature and applying standard formulae for the integrated loss rate (Longair 2010); this of course does not take into account line cooling, which will be important for low temperatures. Results for the $Q = 2 \times 10^{39}$ W jet are shown in Fig. 7. As can be seen, the synchrotron losses for this source, which dominate over the other two processes, are

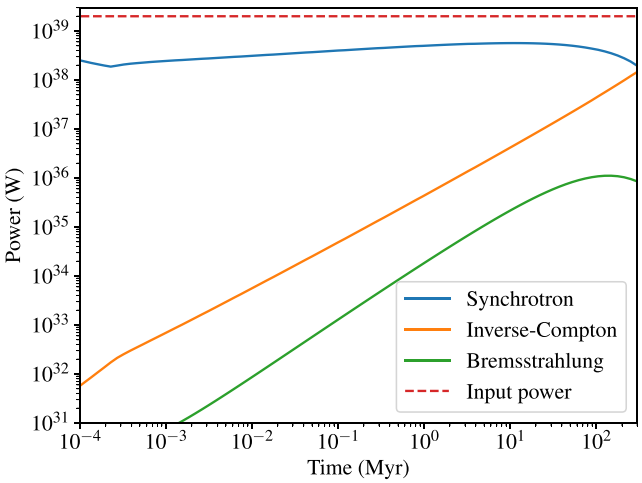

Figure 7. Radiative losses compared to the input jet power as a function of time for the $Q = 2 \times 10^{39}$ W jet discussed in the text. Plotted are the (constant) jet power, the synchrotron loss rate from the lobes, the inverse-Compton loss rate from the lobes at $z = 0$, and the thermal bremsstrahlung loss rate from the shocked shell.

consistently of the order of 10 per cent of the total jet power; neglecting this term in considering the dynamics will cause us to overestimate the volume of the lobes by a modest amount, though of course the uncertainties this imposes on the dynamical model are probably negligible compared to those on our assumptions on other model parameters. The fraction P/Q is a weak function of Q, in the sense that it is lower for lower jet powers. For this particular source, synchrotron emission is the dominant loss process except at the very end of the model run, but at high redshift, it is easily possible for the inverse-Compton losses to exceed the input jet power at late stages of a source's lifetime, and in such a case, the dynamics could well be more significantly affected. Synchrotron losses would also be significantly higher for values of ζ closer to 1. A fully self-consistent treatment of radiative losses in solving for the dynamics would add significantly to the complexity of the code and I defer the development of such a model to a future paper.

3.8 Source ensembles

In this section, I use the model to generate evolutionary tracks in terms of observable quantities for active sources. A standard plot in the study of radio galaxy evolution is the power-linear size ('*P–D*') diagram of Baldwin (1982); here I also consider the spectral index/linear size ('α–*D*') diagram.

To populate such a plot, I consider sources with jet powers in the range 10^{36}–10^{40} W; I take 13 discrete values of Q in this range, including the endpoints, evenly spaced in log space. I consider 10 different universal pressure profile environments with M_{500} uniformly distributed in log space between 10^{13} and $10^{15} M_{\odot}$, and allow the sources to evolve in these environments with constant jet power for 500 Myr (chosen because it traces even the lowest power sources out to Mpc sizes; the linear size axis for the models is truncated, as for some high-power sources in poor environments, the source can grow to scales of tens of Mpc in this time). As before, I assume $\zeta = 0.1$ and $\xi = 0.4$. Fig. 8 shows the results. Overplotted on this figure are grey dots representing the 3CRR sources of Laing, Riley & Longair (1983).[3] A direct comparison between the model plots and a sample such as 3CRR is difficult for a number of reasons. First, 3CRR spans the redshift range from $z = 0$ to 2, and we know from above that the effects of the CMB are important at high z: accordingly I carry out the synchrotron calculation for both $z = 0$ and 2 to show the maximum possible difference. Secondly, real sources are projected (i.e. their measured physical size is shorter than their true physical size); for most sources, this will introduce a small systematic error which I do not consider further here. And thirdly, as I will discuss below, the data available for these sources are not always of high quality. Nevertheless some useful conclusions can be drawn.

Looking first at the model sources in the $z = 0$ *P–D* plot of Fig. 8, we see that the range in radio luminosity is mostly driven by the input jet power; swathes of colour representing the different jet powers are clearly distinguishable across the diagram. However, up to one order of magnitude dispersion at $z = 0$ is caused by the different source environments by the time the sources have grown to 100-kpc scales and reached their maximum radio luminosity. This is most clearly visible on the plot for the lowest power sources, but a similar dispersion is present for all jet powers though it decreases somewhat with jet power. Qualitatively and quantitatively, this dispersion supports the conclusions of Hardcastle & Krause (2013). Jet power can indeed be inferred crudely from luminosity alone, but there is a degeneracy between jet power and environment such that errors of up to an order of magnitude can be made in doing so, *if* there is no relationship in general between jet power and environment richness, a point that I shall return to below.

The range of jet powers used here were intended to represent a plausible range of jet powers for objects in the 3CRR sample, and they succeed in reproducing the range of radio luminosities very well. We may conclude, subject to the model assumptions, that the 3CRR jet power range is more or less the same as the input one, and in particular that few jets in the Universe exceed powers of 10^{40} W. As such jet powers would imply accretion rates of *at least* (i.e. with 100 per cent efficiency), a few solar masses a year over time-scales of order 10^8 yr, this upper limit appears consistent with observed black hole masses in the most massive galaxies at the present day. The main effect of going from $z = 0$ to 2 on the *P–D* diagram is to predict a stronger downturn of the luminosity with size for large sizes, as I have already noted, and this also appears to be consistent with the 3CRR observations in that there are no large objects at the maximum radio luminosity, which would require much higher jet powers in these models (since the most luminous objects in 3CRR are also at the highest redshifts). Of course, other effects, including shorter source lifetimes at high z, could be responsible for this effect. Going to high z also increases the environmental effect on radio luminosity for a given jet power, particularly at late times, again because of the additional effects of the CMB (we do not model any redshift evolution of the universal pressure profile). For the lowest power sources, the scatter in luminosity for a given jet power increases to almost two orders of magnitude in radio luminosity.

The spectral index plots in Fig. 8 present a more complex picture and a less good agreement with the observational data. Looking first at the models, we see that at $z = 0$ sources go from flat spectrum, $\alpha < 0.7$ on scales $\lesssim$ 10kpc (with lower power sources being flatter in spectrum) to steep spectrum, $0.8 < \alpha < 0.95$, on 100-kpc scales. In the steep-spectrum regime, the main driver appears to

[3] Data are taken from the compilation at http://3crr.extragalactic.info/.

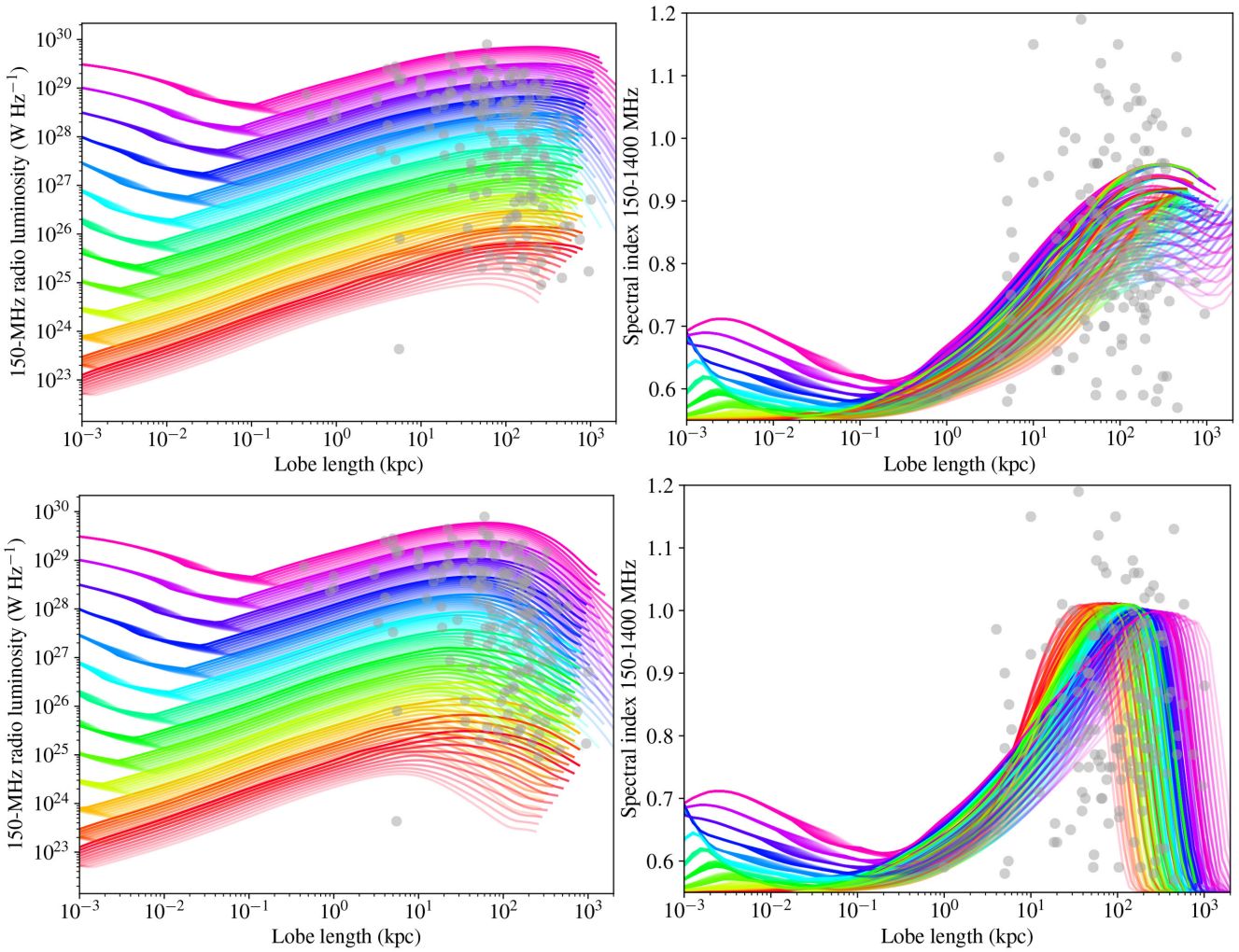

Figure 8. Tracks in the *P*–*D* and α–*D* diagrams for ensembles of sources at $z = 0$ (top panels) and $z = 2$ (bottom panels). All panels show the evolution up to $t = 500$ Myr of sources with 13 different jet powers evenly spaced in log space between 10^{36} and 10^{40} W; jet power is indicated by the rainbow colours (red is low power and violet is high power). Each jet power is placed in a universal pressure profile with 10 different values of M_{500} between 10^{13} and 10^{15}M$_\odot$, evenly spaced in log space, indicated by the brightness of the rainbow colour (faint is low mass and bright is high mass). Overplotted on all plots are the rest-frame 150-MHz luminosities and the observer-frame 178–750 MHz spectral indices of the 3CRR sample, plotted against half their physical (projected) size. See the text for more details.

be environmental density in the sense that the most massive environments show the steepest spectra irrespective of jet power. At $z = 2$, we see quite a different picture for the large sources where spectra are first steep and then flatten again: as noted above, this is because old material is aged out of even the 150-MHz rest-frame band by inverse-Compton losses at this redshift. The dispersion in spectral index for a given band is driven mostly by jet power in this regime (because higher jet powers will imply higher magnetic field strengths for a given size), but within bands of jet power environment also plays a role. Roughly speaking, the environmental dispersion in α is of order ± 0.05, so this is a small effect.

The comparison with the 3CRR sources is less good here at least partly because the available data do not match what I have modelled. What is plotted for the real sources is the 178–750 MHz observer-frame spectral index as tabulated by Laing et al. (1983), whereas what I calculate, to facilitate comparison with more modern data, is the rest-frame 150–1400 MHz index. For high-z sources, one would expect the true spectral indices to be steeper than what is calculated from the model for a given source size and jet power: for low-z sources, they might be a little flatter. In addition, the 750-MHz flux densities used for the calculation originate from the work of Kellermann, Pauliny-Toth & Williams (1969) and have non-negligible error bars. It is beyond the scope of this paper to derive improved 3CRR integrated spectra, though the data exist to do so using modern surveys like The National Radio Astronomy Observatory Very Large Array Sky Survey (NVSS) (Condon et al. 1998) and the LOFAR Multifrequency Snapshot Sky Survey (MSSS) (Heald et al. 2015). Of course, in addition, real radio galaxy spectra may be affected by other physical effects, such as self-absorption (although that will be irrelevant for most large 3CRR sources) and relativistic beaming in the core, jets, and hotspots. A couple of qualitative conclusions may nevertheless be drawn. First, the large number of large sources in 3CRR with flat spectra and comparatively large physical sizes may be partly explained by inverse-Compton losses at higher z, as shown in the bottom right panel of Fig. 8. Secondly, from the results of Section 3.5, the scatter in the integrated spectral index in real sources with respect to the model prediction, and in particular, the number of sources with spectra steeper than the model can

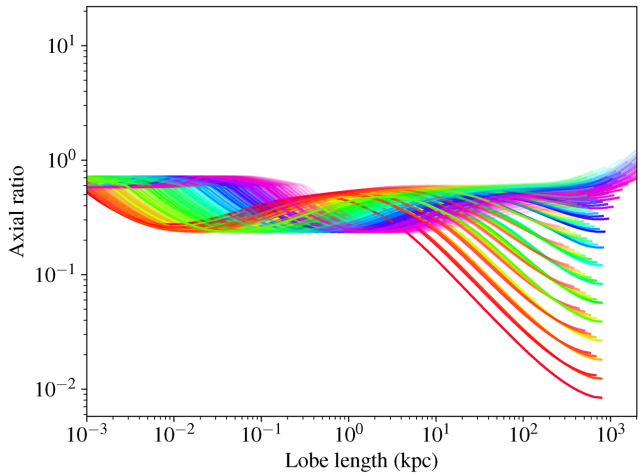

Figure 9. Tracks in the axial ratio/linear size diagram. Colours as in Fig. 8.

account for, may be partly because the spectral index is very sensitive to changes in the jet power over the lifetime of a source – if we view the behaviour in Fig. 5 as the response to a step change in Q, then it is clear that smaller decreases in Q could produce smaller but still significant steepening. It is also possible that variations in the injection index from the $q = 2.1$ assumed throughout this modelling could be responsible for the steep observed spectra in some 3CRR sources; this effect is not present in our models.

These results on tracks in the P–D diagram can be compared to those of Kaiser et al. (1997), Blundell et al. (1999), or Turner et al. (2018); the most directly comparable earlier plots are in figs 13 and 14 of Blundell et al. (1999, note that they use one-sided jet powers, total source sizes, and radio luminosities in W Hz^{-1} sr^{-1}). It is worth emphasizing that all of these comparison models agree in the broad range of luminosities that are inferred for a given jet powers and source size, implying good convergence on the basic source physics despite differences in the detailed modelling. The models of this paper however show radio luminosities that are still rising at source sizes ∼10 kpc, whereas in the Kaiser et al. (1997) or Blundell et al. (1999) analytical models the luminosity is monotonically decreasing with time. This is a consequence of the power-law atmosphere assumption in the earlier work (Section 1.3).

3.9 Lobes and plumes

In Fig. 9, I plot the axial ratio of the sources from the previous subsection as a function of lobe length, where I define the axial ratio as the diameter of the lobe divided by its length, and estimate lobe diameters by taking the volume of the lobe to be a cylinder with length R and volume given by equation (5). Sources show a characteristic evolution with time, with a constant axial ratio at early times, then a drop to smaller (thinner) values, then an increase to a peak value around 0.3–0.4, and then in most but not all cases a drop again. Sources that are more powerful or in poorer environments peak later than lower power sources or those in richer environments. What is striking about this plot is the existence of a number of low-power sources in the richest environments that have low axial ratios (i.e. long and thin lobes). This is simply a consequence of the slower transverse growth of these sources coupled with the behaviour of equation (5) which implies that the energetics of these low-power, high-density systems is more easily dominated by the swept-up gas. However, it is certainly qualitatively reminiscent of the evolution of plumes in FRI sources (including wide-angle tail sources) in dense environments as discussed in Section 1.2), and the jet powers involved are consistent with those of such sources, which at least in some cases are still known to drive shocks on large scales (e.g. Simionescu et al. 2009). Modelling the luminosity evolution of these sources in a way consistent with the constraints from observation would entail taking account of entrained material (Section 1.2) and, as the model does not do this, their positions on Fig. 8 should be treated with caution.

4 POPULATIONS AND LIFETIMES

4.1 Model setup

In this section, I use the model to consider the effects of distributions of model parameters and selection effects on observed source properties.

I generate sources with the basic model parameters of the previous subsections (in particular $\xi = 0.4$ and $\zeta = 0.1$). It is not the purpose of this paper to try to match real cosmological distributions of environment, redshift or jet power – at this point, we simply do not know these distributions (or, crucially, their dependencies on each other) well enough for this to be a useful exercise. Instead, I draw sources' redshift from a uniform distribution over $0 \leq z < 4$, jet powers from a uniform distribution in log space over $36 \leq \log_{10}(Q/\mathrm{W}) < 40$, and environment from a uniform distribution in log space such that $13 \leq \log_{10}(M_{500}/M_{\odot}) < 15$. Sources are also assigned a random angle to the line of sight distributed such that $p(\theta) = \sin(\theta)$ for $0 < \theta < \pi/2$; the apparent size of a source is then $R \sin\theta$.

The crucial choice here is the selection of the distribution of source lifetimes. To model source evolution, we need to consider a period in the immediate past in the frame of each radio source that is long compared to the typical source lifetime (here we choose 1 Gyr). Sources are then assumed to be triggered at uniformly distributed times in that time range – there is no explicit cosmological evolution in the model – so that at the time of 'observation' each source may have switched on with equal probability between 0 and 1000 Myr ago. Every source is evolved according to the model up to the time of observation. The crucial choice concerns the time period over which the source has an active jet during the modelling time. Each source is assigned a lifetime T and is modelled as a remnant (Section 3.5) for $t > T$. In what follows, I consider two models: (i) T is drawn from a uniform distribution in linear space between 0 and 500 Myr; and (ii) T is drawn from a uniform distribution in log space in the range $-3 \leq \log_{10}(T/\mathrm{Myr}) < \log_{10}(500)$. 10 000 sources are simulated for each of these two distributions.

Once the sources' dynamics have been evolved up to the time of observation, I then apply the corrections for radiative and adiabatic losses described in Section 2.3, computing them only for the final time-step of the simulation. I choose an 'observing' frequency of 150 MHz as the reference frequency and also compute the corrections needed to calculate *observer's-frame* spectral index between 150 and 1400 MHz. When these calculations are done, many sources (where the source has been in the remnant phase for a long time at the time of observation) have 150-MHz luminosities which are reduced by the loss corrections to negligible values, and hence would not be detected by any real observation: these sources are considered 'dead'. Sources for which this is not true, and so might in principle be detected, even if they are remnants, are referred to as 'live' in what follows.

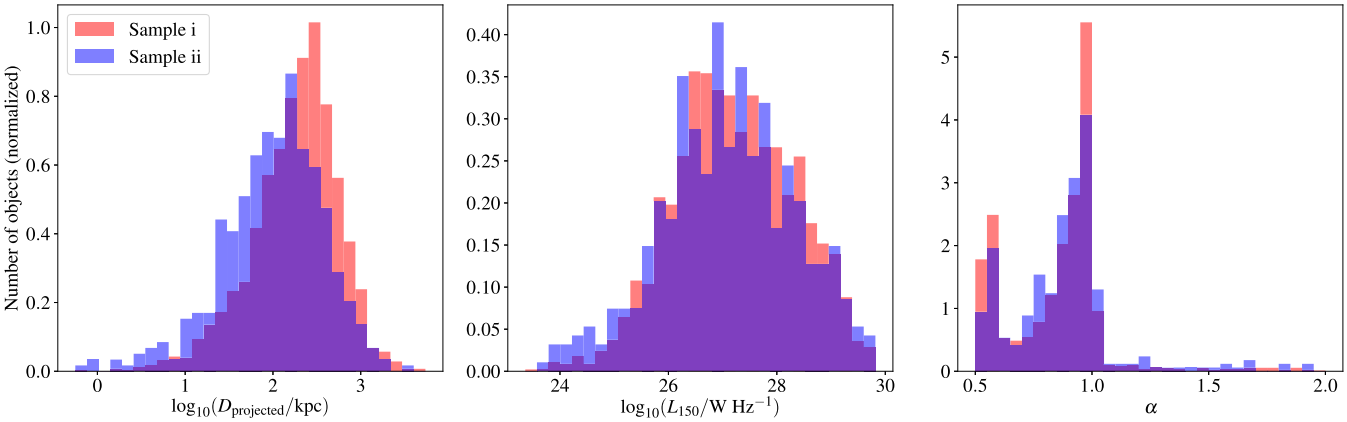

Figure 10. Histograms of key observables for the simulated populations. The left-hand and centre panels show the full range of the distributions in linear size and radio luminosity for the observationally selected subsamples of Samples (i) and (ii). The range in the right-hand panel has been chosen to allow the distribution of spectral indices between 150 and 1400 MHz in the non-remnant population to be seen – the tail of very steep spectral indices, associated with extreme remnants, continues to very steep, in practice unobservable, spectral indices.

I can then convert intrinsic to observed quantities using a standard flat Λcold dark matter cosmology with $H_0 = 70\,\mathrm{km\,s^{-1}}$, $\Omega_\mathrm{m} = 0.3$, and $\Omega_\Lambda = 0.7$ and calculate the observed 150-MHz flux density and angular size. This allows me to mimic observational selection criteria, which give us both a flux density and a surface brightness limit. To roughly match bright samples derived from LOFAR surveys (see e.g. Hardcastle et al. 2016), I choose a flux limit of 10 mJy and a surface brightness limit of a few times the rms noise in LOFAR imaging of ∼100 μJy beam^{-1} with a 6-arcsec Gaussian restoring beam. Only 'live' sources which meet the flux and surface brightness limits are included in the samples I analyse; the intention is that the selection effects in real data are at least roughly modelled in the simulations.

Below I discuss some of the results of this modelling for the two lifetime distributions considered.

4.2 Basic properties and the effects of lifetime distribution

Sample (i), where the lifetime distribution is uniform in linear space, contains 3453 'live' sources out of 10 000 (34 per cent), of which 2112 are selected by the observational criteria. Sample (ii), where the lifetime distribution is uniform in log space (and therefore there are many more short-lived sources), contains only 841 live sources, of which 443 are observable. The mean lifetime (and therefore the total injected AGN energy) is of course shorter in Sample (ii) and so no physical conclusions can be drawn from the different source numbers.

Fig. 10 shows histograms of the distributions of key observable source parameters for the two samples. We can see that the two choices for lifetime distributions produce almost identical distributions of L_{150} and α but clearly distinct source size distributions – in the sense that Sample (ii), with typically shorter lifetimes, produces many more small sources. The median projected size in observable sources in Sample (ii) is 117 kpc, whereas it is 206 kpc in Sample (i). Note that this difference is not nearly as extreme as the difference in the median lifetimes for the parent samples – 250 Myr versus 0.7 Myr – because most of the short-lifetime sources are low in luminosity and/or die long before they can be observed. Observational selection effects favour large, bright sources. Nevertheless, this plot illustrates the importance of the lifetime distribution in determining the size distribution. If other controlling parameters such as the environment and jet power distributions were known, the lifetime distribution could in principle be constrained from observations.

4.3 Remnants

Godfrey et al. (2017) have recently addressed the question of the remnant fraction expected in sensitive observations. I do not propose to repeat all of their analysis here, but it is interesting to look at the effects of our different modelling and selection on the expected numbers of remnants.

The observed subsamples of Samples (i) and (ii) have slightly different total remnant fractions, respectively, 20 per cent and 34 per cent (the statistical error on the fraction in Sample (ii) is roughly 3 per cent, so this difference is significant). Again we see that the lifetime distribution has an effect. It is not hard to see why Sample (ii), which contains the same number of sources but with shorter lifetimes, has a higher remnant fraction. Thus, the remnant fraction in principle constrains not just the physics of post-jet source evolution but also the lifetime distribution.

Fig. 11 shows the remnant fraction as a function of redshift for Sample (i). (Sample (ii) shows similar trends but with poorer statistics and we do not consider it further here.) I plot both the total observed sample, and, for comparison, the distribution of luminous objects with $L_{150} > 3 \times 10^{25}$ W Hz^{-1}, a luminosity above which the *P–D* diagram is well sampled for active sources. We can see that the remnant fraction is a strong function of redshift. This is due to a combination of the faster CMB inverse-Compton loss rates at high redshift, as discussed above, with observational selection effects that reduce the numbers of low-luminosity high-z sources detected. At $z < 1$, the fraction of remnants is 37 per cent (31 per cent above 3×10^{25} W Hz^{-1}). It drops to less than 10 per cent for $1 < z < 2$ and is basically negligible at $z > 2$. Both the remnant fraction and the trend with redshift are broadly consistent with the results of Godfrey et al. (2017), who used a uniform distribution of source lifetimes up to 200 Myr, despite the many differences in the modelling and assumptions about source and power distributions, but it is worth noting that in the Godfrey et al. (2017) models remnants are comparable to, or even outnumber active sources at low z, whereas in the models of this paper they never do so. Around

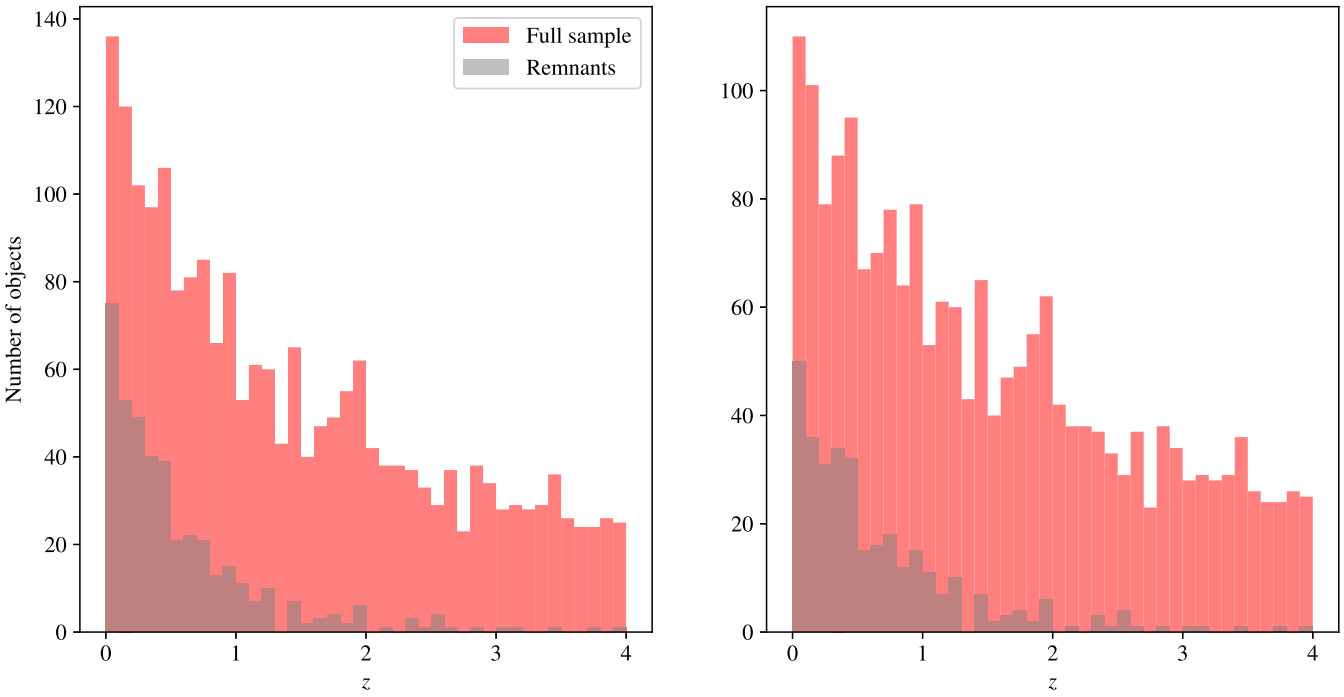

Figure 11. The redshift distribution of all sources and of remnant sources in Sample (i) as discussed in the text. Left-hand panel: all luminosities are shown. Right-hand panel: only sources with $L > 3 \times 10^{25}$ W Hz^{-1} are shown.

80 per cent of the remnant sources have 'ultrasteep' observer-frame 150–1400 MHz spectral index $\alpha > 1.5$.

4.4 The radio power/jet power relation

The modelling allows me to investigate the 'observed' radio luminosity to jet power relation. Here, I use exclusively the observed subsample of Sample (i), since the results should not in this case be dependent on the lifetime distribution.

Fig. 12 (left) shows a scatter plot of radio luminosity as a function of Q. Remnants are clear outliers, as expected, but the non-remnant sources show a good linear correlation, albeit with about two orders of magnitude scatter (as indicated by lines on the figure) between the two quantities. Also plotted are the relationships of Willott et al. (1999) for two values of their factor f, $f = 1$ and 20; we see that $f = 1$ substantially overpredicts the radio luminosity for a given jet power, but larger values of f do reasonably well at reproducing the predictions of the model.

The major factor driving the scatter in the relation is redshift, as can be seen from the colour coding in Fig. 12; high-z sources have significantly lower radio luminosity for a given Q. This trend is a result of the increased inverse-Compton losses at higher redshifts, bearing in mind that observationally selected sources are biased towards large sizes. If we consider sources in a narrow redshift band, e.g. as in the right-hand plot of Fig. 12, then the remaining driver of scatter is, as expected, environment, together with other sources of scatter such as evolutionary state. For $z < 0.5$, there is roughly 0.4 dex (rms) of scatter about the relation

$$L_{150} = 3 \times 10^{27} \frac{Q}{10^{38}\ \mathrm{W}}\ \mathrm{W\ Hz^{-1}} \qquad (22)$$

where the normalization is estimated directly from the simulated observations of non-remnant sources. The Willott et al. (1999) relation with $f = 5$ also fits the data reasonably well. Our best-fitting relation is also very consistent with the regression line of Ineson et al. (2017) for their sample of FRIIs with very similar jet powers and overall physical properties to those modelled here, and, as they note, therefore also consistent with observational constraints by Daly et al. (2012) and with the modelling of Turner & Shabala (2015).

The good agreement between these different observational and theoretical models is striking and suggests that inference of jet powers from radio luminosities can be done in a reasonably robust manner in real samples of FRIIs with known redshifts. However, the modelling also makes it clear that taking environment and age into account is important to get a more accurate result – there is still nearly an order of magnitude difference between the lower and upper envelopes of the right-hand plot of Fig. 12 – and that special classes of sources, such as outliers or extreme giants, will be outliers on any regression. Estimates of the active jet power of remnants or even the largest giants naively using the relation of equation (22) would lie below the true Q values by several orders of magnitude.

Finally, it is important to note yet again that the radio luminosities I calculate in the model depend on model assumptions on quantities like ζ and the jet injection index q. If these have some intrinsic scatter, or worse still if they are found to depend on jet power Q itself in real sources, then there will be corresponding dispersion or bias in inferences of jet power using the model. The modelling here thus demonstrates the importance of constraining the distributions of these quantities and their relationship to jet power in large observational samples.

4.5 Radio luminosity and environment

Ineson et al. (2013, 2015) are the latest in a line of authors to report a correlation between radio luminosity and some measure of cluster richness – in their particular case between radio luminosity and X-ray luminosity of the host environment for the low-excitation radio galaxy population only. I searched for any such relation in the

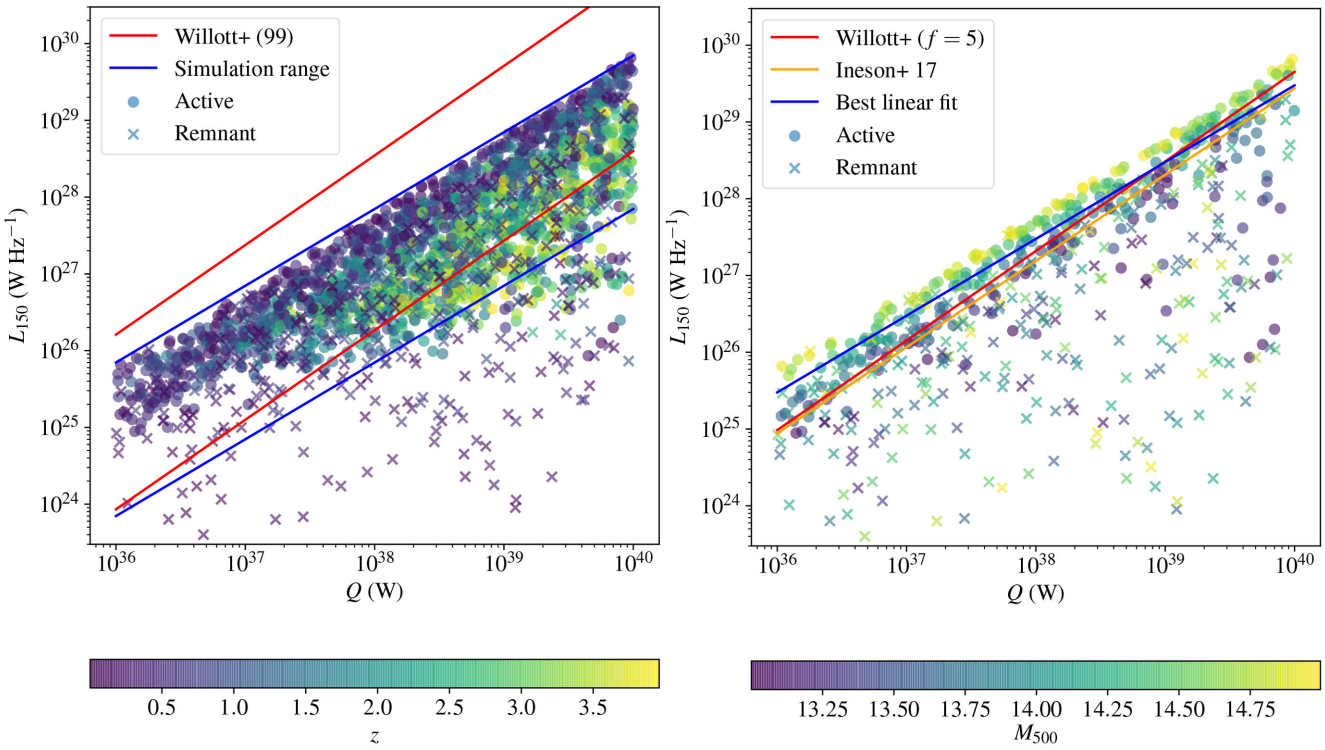

Figure 12. Radio luminosity as a function of jet power. Left-hand panel: all observed sources from Sample (i), colour coded by redshift. Overplotted in blue are lines bounding the relation for active sources ($L_{150} = 7 \times 10^{27}(Q/10^{38}\,\mathrm{W})\,\mathrm{W\,Hz^{-1}}$ and $L_{150} = 7 \times 10^{25}(Q/10^{38}\,\mathrm{W})\,\mathrm{W\,Hz^{-1}}$) and in red are the Willott et al. (1999) relation for $f = 1$ (top) and $f = 20$ (bottom). Right-hand panel: only the $z < 0.5$ sources from Sample (i), colour coded by M_{500}. Overplotted in blue is the best-fitting linear relation, $L_{150} = 3 \times 10^{27}(Q/10^{38}\,\mathrm{W})\,\mathrm{W\,Hz^{-1}}$, in red is the Willott et al. (1999) relation with $f = 5$, and in orange is the relation of Ineson et al. (2017).

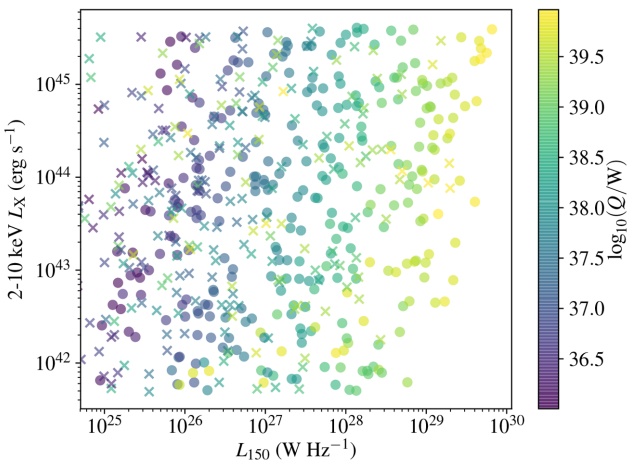

Figure 13. Cluster X-ray luminosity as a function of radio luminosity for $z < 0.5$ objects in the observed subsample [the orientation of the plot matches Fig. 6 of Ineson et al. (2015).] Remnant sources are marked with crosses and active sources are filled circles. Sources are colour coded with their jet power so that trends with this quantity are visible.

simulated observations of Sample (i) at $z < 0.5$, i.e. roughly matched to the redshift range of Ineson et al. (2015). No such relationship is found in the simulated data (Fig. 13), where I map M_{500} on to cluster X-ray luminosity using the relationship of Pratt et al. (2009), though the simulated data span exactly the X-ray and radio luminosity range observed by Ineson et al. For a given jet power, of course, the cluster mass drives ∼1 order of magnitude of scatter in the radio luminosity, but most of the variation in radio luminosity is due to variation in Q. This supports the argument of Ineson et al. (2015) that some intrinsic relationship between the jet power and the cluster mass might be required to produce such a correlation. In the simulations of this section, a jet of any power can be switched on in an environment of any richness, and the only observational selection effect is whether it produces a radio source bright enough to be observed in the sample. In reality, at least for sources where the hot gas is the source of accreting material, we might expect an intrinsic Q–M_{500} correlation – and perhaps also a lifetime–M_{500} correlation? – which could drive the sort of result seen by Ineson et al. (2015). This in turn might be expected to affect the scatter in and the observational slope of jet power/radio luminosity plots such as those discussed in the previous section.

4.6 The age–size relation

The apparent (projected) linear size of a source is expected to be an indicator of age, but is affected by many other factors, including projection. Fig. 14 shows the relationship for the observed subset of Sample (i). Sources with ages of a few hundred Myr can have apparent linear sizes of anywhere between a few and a few hundred kpc. Jet power (as shown on the figure) and environment affect the position of a source on this plot, but the unknown projection angle makes the length of any given source a poor measure of its age. Constraining the projection angle for large samples will require measurements of the side-to-side depolarization ratio (Laing 1988; Garrington et al. 1988) which will only be possible for well-resolved sources [this ratio can be measured in numerical simulations

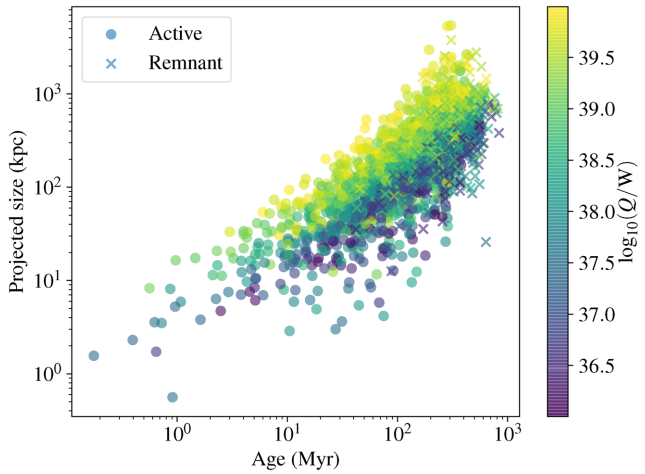

Figure 14. Source linear size as a function of age for the observed subsample, colour coded by jet power.

(Hardcastle & Krause 2014), but is not currently predicted by the model of this paper] or of jet sidedness or prominence, which give more indirect measurements of the angle and again require high resolution. For sources with the required multiwavelength, resolved radio images, direct spectral ageing measurements will also be possible, so it seems unlikely that direct estimates of age from the size will ever be useful. The most reliable estimate of a source age in the absence of such resolved imaging might be derived from estimating the jet power from relationships such as that of Section 4.4 and then inferring the age from the total energetic content of the lobes, which depends only weakly on the true lobe linear size.

5 SUMMARY AND CONCLUSIONS

This paper has presented a new 'semi-analytical' model of powerful radio galaxy evolution, which centres around a couple of simple differential equations to model the evolution of the shock front around FRII-type lobes, making use of a number of simplifying assumptions derived from 2D and 3D numerical modellings. In the reference models, I assume a light, electron–positron jet, no non-radiating particles in the lobes, and a magnetic field energy density about a tenth of that in the radiating particles – all based on existing observational constraints. Unlike many existing models, I make no assumptions about self-similar expansion of the lobes or shocks. These equations are solved numerically, in principle for a general spherically symmetrical environment, in practice for isothermal β models or the 'universal pressure profile' of Arnaud et al. (2010); the radio luminosity and spectral evolution of the simulated sources can then be determined in post-processing. I show good agreement between the dynamics of the model and earlier numerical simulation work, as expected since the model's assumptions are based on numerical simulations. The model can reproduce the broad features of the evolution of the synchrotron luminosity also seen in numerical models. The evolution of the integrated spectrum of a source from flat to steep, as seen observationally, is also reproduced. PYTHON code to carry out all of these steps is publicly available at https://github.com/mhardcastle/analytic.

Key results of the paper are as follows:

(i) The typical integrated spectrum of an aged source is smoothly curved over two decades of radio frequency, rather than being a broken power law (Section 3.4).

(ii) The relatively low magnetic field strengths in the fiducial models imply an important role for inverse-Compton losses at high z. Thus, the radio luminosity evolves more strongly with time, and is in general lower for a given jet power, at high redshift than at $z = 0$; this qualitative behaviour agrees with earlier work, but the quantitative effect will depend on assumptions about magnetic field strength (Section 3.4).

(iii) Remnant sources, after the jet has switched off, show a rapid evolution of radio luminosity and spectral index due to the cessation of injection of new flat-spectrum electrons combined with radiative and adiabatic losses of the previously existing population (Section 3.5). This is consistent with recent work by Godfrey et al. (2017).

(iv) In early stages of source evolution, a steep spectrum for a given lobe length is a good marker of a rich environment. However, radio galaxies in general, and high-z sources in particular, can move to a low-luminosity, flat-spectrum state at late times where the most recently injected electrons dominate the integrated radio emission. Thus, selection of either high-z radio sources or sources in rich environments by their spectral indices needs to be carried out with care (Sections 3.4 and 3.8).

(v) If jet power and environment are unrelated, which may not be the case in real objects, jet power is the main driver of radio luminosity variations. The plausible two orders of magnitude variation in cluster mass that I model, however, gives rise to one to two orders of magnitude variation in radio luminosity for a given jet power and redshift (Section 3.8). Thus simple inference of the jet power from radio luminosity is unsafe.

(vi) Studies of simulated sources with different lifetime distributions shows that the distribution of source lifetimes has a significant effect on both the source length distribution and the fraction of remnant sources expected in observations (Section 4.2). The remnant fraction is expected to be low (∼30 per cent) even at low redshift and low observing frequency due to the rapid luminosity evolution of remnants, and to tend rapidly to zero at high redshift due to inverse-Compton losses (Section 4.3).

(vii) Simulated observations reproduce a strong correlation between low-frequency radio luminosity and jet power (Section 4.4), which is in excellent agreement with recent observational work, but only a poor correlation between source apparent size and age (Section 4.6). Source redshift, age, and environment all also affect the luminosity.

(viii) No radio luminosity/environment correlation is expected in samples in which the jet power and environment are independent. The observation of such a correlation in real data suggests a physical relationship between jet power and hot-gas environment, perhaps mediated by the source of fuel for accretion and/or by black hole mass (Section 4.5).

Although the model described here is encouragingly consistent with both observations and numerical models of larger samples, it is clear that its adjustable parameters should be refined by further detailed study of small numbers of sources in the regime that it best describes. In a forthcoming paper, Mahatma et al. will compare the model predictions with radio and X-ray observations of two powerful cluster-centre FRII sources. At a later stage, we hope to apply it to large samples of powerful sources generated from, for example, LOFAR surveys observations (Hardcastle et al. 2016; Shimwell et al. 2017) with the aim of inferring the kinetic luminosity function of powerful jets and hence the work being done by radio-loud AGN on their environments at the present day.

ACKNOWLEDGEMENTS

I am grateful to Judith Croston, Martin Krause, and Judith Ineson for helpful discussion of many of the topics covered in this paper, and to Vijay Mahatma, Martin Krause, and Judith Croston for helpful comments on earlier drafts. I thank an anonymous referee for constructive comments.

I acknowledge support from the UK Science and Technology Facilities Council [ST/M001008/1]. This research has made use of the University of Hertfordshire high-performance computing facility (http://stri-cluster.herts.ac.uk/). This research made use of ASTROPY, a community-developed core PYTHON package for astronomy (Astropy Collaboration et al. 2013) hosted at http://www.astropy.org/, and of TOPCAT (Taylor 2005).

REFERENCES

Arnaud M., Pointecouteau E., Pratt G. W., 2005, A&A, 441, 893
Arnaud M., Pratt G. W., Piffaretti R., Böhringer H., Croston J. H., Pointecouteau E., 2010, A&A, 517, A92
Astropy Collaboration, et al., 2013, A&A, 558, A33
Baldi R. D., Capetti A., Giovannini G., 2015, A&A, 576, A38
Baldwin J. E., 1982, in Heeschen D. S., Wade C. M., eds, IAU Symp. Vol. 97, Extragalactic Radio Sources. D. Reidel Publishing Co., Dordrecht, p. 21
Barthel P. D., Arnaud K. A., 1996, MNRAS, 283, L45
Bicknell G. V., 1994, ApJ, 422, 542
Bicknell G. V., 1996, in Hardee P. E., Bridle A. H., Zensus J. A. eds, ASP Conf. Ser. Vol. 100, Energy Transport in Radio Galaxies and Quasars. Astron. Soc. Pac., San Francisco, p. 253
Blundell K. M., Rawlings S., Willott C. J., 1999, AJ, 117, 677
Bowman M., Leahy J. P., Komissarov S. S., 1996, MNRAS, 279, 899
Brienza M. et al., 2017, A&A, 606, A98
Cavagnolo K. W., McNamara B. R., Nulsen P. E. J., Carilli C. L., Jones C., Bîrzan L., 2010, ApJ, 720, 1066
Cavaliere A., Fusco-Femiano R., 1978, A&A, 70, 677
Condon J. J., Cotton W. D., Greisen E. W., Yin Q. F., Perley R. A., Taylor G. B., Broderick J. J., 1998, AJ, 115, 1693
Croston J. H., Hardcastle M. J., 2014, MNRAS, 438, 3310
Croston J. H., Hardcastle M. J., Birkinshaw M., 2005, MNRAS, 357, 279
Croston J. H., Hardcastle M. J., Kharb P., Kraft R. P., Hota A., 2008, ApJ, 688, 190
Croston J. H., et al., 2009, MNRAS, 395, 1999
Croston J. H., Ineson J., Hardcastle M. J., 2018, MNRAS, submitted
Daly R. A., Sprinkle T. B., O'Dea C. P., Kharb P., Baum S. A., 2012, MNRAS, 423, 2498
English W., Hardcastle M. J., Krause M. G. H., 2016, MNRAS, 461, 2025
Fanaroff B. L., Riley J. M., 1974, MNRAS, 167, 31P
Gallant Y. A., 2002, in Guthmann A. W., Georganopoulos M., Marcowith A., Manolakou K., eds, Relativistic Flows in Astrophysics. Lecture Notes in Physics, Vol. 589, Springer-Verlag, Berlin, p. 24
Garrington S., Leahy J. P., Conway R. G., Laing R. A., 1988, Nature, 331, 147
Godfrey L. E. H., Morganti R., Brienza M., 2017, MNRAS, 471, 891
Hardcastle M. J., 2004, A&A, 414, 927
Hardcastle M. J., 2013, MNRAS, 433, 3364
Hardcastle M. J., Krause M. G. H., 2013, MNRAS, 430, 174
Hardcastle M. J., Krause M. G. H., 2014, MNRAS, 443, 1482
Hardcastle M. J., Sakelliou I., 2004, MNRAS, 349, 560
Hardcastle M. J., Worrall D. M., 2000, MNRAS, 319, 562
Hardcastle M. J., Birkinshaw M., Worrall D. M., 1998, MNRAS, 294, 615
Hardcastle M. J., Birkinshaw M., Cameron R., Harris D. E., Looney L. W., Worrall D. M., 2002, ApJ, 581, 948
Hardcastle M. J., Worrall D. M., Birkinshaw M., Laing R. A., Bridle A. H., 2005, MNRAS, 358, 843
Hardcastle M. J., et al., 2016, MNRAS, 462, 1910
Harwood J. J., 2017, MNRAS, 466, 2888
Heald G. H., et al., 2015, A&A, 582, A123
Ineson J., Croston J. H., Hardcastle M. J., Kraft R. P., Evans D. A., Jarvis M., 2013, ApJ, 770, 136
Ineson J., Croston J. H., Hardcastle M. J., Kraft R. P., Evans D. A., Jarvis M., 2015, MNRAS, 453, 2682
Ineson J., Croston J. H., Hardcastle M. J., Mingo B., 2017, MNRAS, 467, 1586
Jaffe W. J., Perola G. C., 1973, A&A, 26, 423
Jetha N. N., Hardcastle M. J., Ponman T. J., Sakelliou I., 2008, MNRAS, 391, 1051
Kaiser C. R., Alexander P., 1997, MNRAS, 286, 215
Kaiser C. R., Best P. N., 2007, MNRAS, 381, 1548
Kaiser C. R., Dennett-Thorpe J., Alexander P., 1997, MNRAS, 292, 723
Kardashev N. S., 1962, SvA, 6, 317
Kataoka J., Stawarz Ł., 2005, ApJ, 622, 797
Kellermann K. I., Pauliny-Toth I. I. K., Williams P. J. S., 1969, ApJ, 157, 1
Kraft R. P., Vázquez S., Forman W. R., Jones C., Murray S. S., Hardcastle M. J., Worrall D. M., Churazov E., 2003, ApJ, 592, 129
Laing R. A., 1988, Nature, 331, 149
Laing R. A., Bridle A. H., 2014, MNRAS, 437, 3405
Laing R. A., Riley J. M., Longair M. S., 1983, MNRAS, 204, 151
Leahy J. P., 1993, in Röser H.-J., Meisenheimer K. ed., Jets in Extragalactic Radio Sources. Springer-Verlag, Heidelberg, p. 1
Ledlow M. J., Owen F. N., 1996, AJ, 112, 9
Longair M. S., 2010, High Energy Astrophysics. Cambridge Univ. Press, Cambridge
Luo Q., Sadler E. M., 2010, ApJ, 713, 398
Mahatma V. et al., 2018, MNRAS, in press
McKean J. P., et al., 2016, MNRAS, 463, 3143
Mocz P., Fabian A. C., Blundell K. M., 2011, MNRAS, 413, 1107
Mullin L. M., Hardcastle M. J., 2009, MNRAS, 398, 1989
Nath B. B., 2010, MNRAS, 407, 1998
Pacholczyk A. G., 1970, Radio Astrophysics. Freeman, San Francisco
Pratt G. W., Croston J. H., Arnaud M., Böhringer H., 2009, A&A, 498, 361
Scheuer P. A. G., 1974, MNRAS, 166, 513
Shimwell T. W., et al., 2017, A&A, 598, A104
Simionescu A., Roediger E., Nulsen P. E. J., Brüggen M., Forman W. R., Böhringer H., Werner N., Finoguenov A., 2009, A&A, 495, 721
Sun M., Sehgal N., Voit G. M., Donahue M., Jones C., Forman W., Vikhlinin A., Sarazin C., 2011, ApJ, 727, L49
Taylor M. B., 2005, in Shopbell P., Britton M., Ebert R., eds, ASP Conf. Ser. Vol. 347, Astronomical Data Analysis Software and Systems XIV. Astron. Soc. Pac., San Francisco, p. 29
Tribble P. C., 1991, MNRAS, 253, 147
Turner R. J., Shabala S. S., 2015, ApJ, 806, 59
Turner R. J., Rogers J. G., Shabala S. S., Krause M. G. H., 2018, MNRAS, 473, 4179
Willott C. J., Rawlings S., Blundell K. M., Lacy M., 1999, MNRAS, 309, 1017
Wykes S., Hardcastle M. J., Karakas A. I., Vink J. S., 2015, MNRAS, 447, 1001

This paper has been typeset from a TEX/LATEX file prepared by the author.